Chapter-4

Vanadate Based Double Perovskite Phosphors: Synthesis and Optimization of Luminescence Properties

Highlights

This chapter presents the investigation on a vanadate double perovskite Sr_2YVO_6 doped with Eu^{3+}, wherein the Eu^{3+} concentration was taken from 1-5 mol%. The synthesis of these phosphors was carried out using the combustion synthesis method by taking urea as a flux. To determine the phase and confirm the crystal structure, XRD was used. Additional structural analysis was performed using FESEM, EDAX and FTIR spectroscopy. The phosphor Sr_2YVO_6 doped with Eu^{3+} underwent irradiation using two different ionizing radiations namely beta and UV rays with varying radiation doses. The PL properties were thoroughly examined for a comprehensive understanding of the phosphor's characteristics. In further analysis, the CIE study was utilized to calculate the chromaticity coordinates and color temperature, exploring the potential application of the material in lighting displays. Overall obtained results give enough evidence that the phosphor under study can be incorporated for displays and TLD applications.

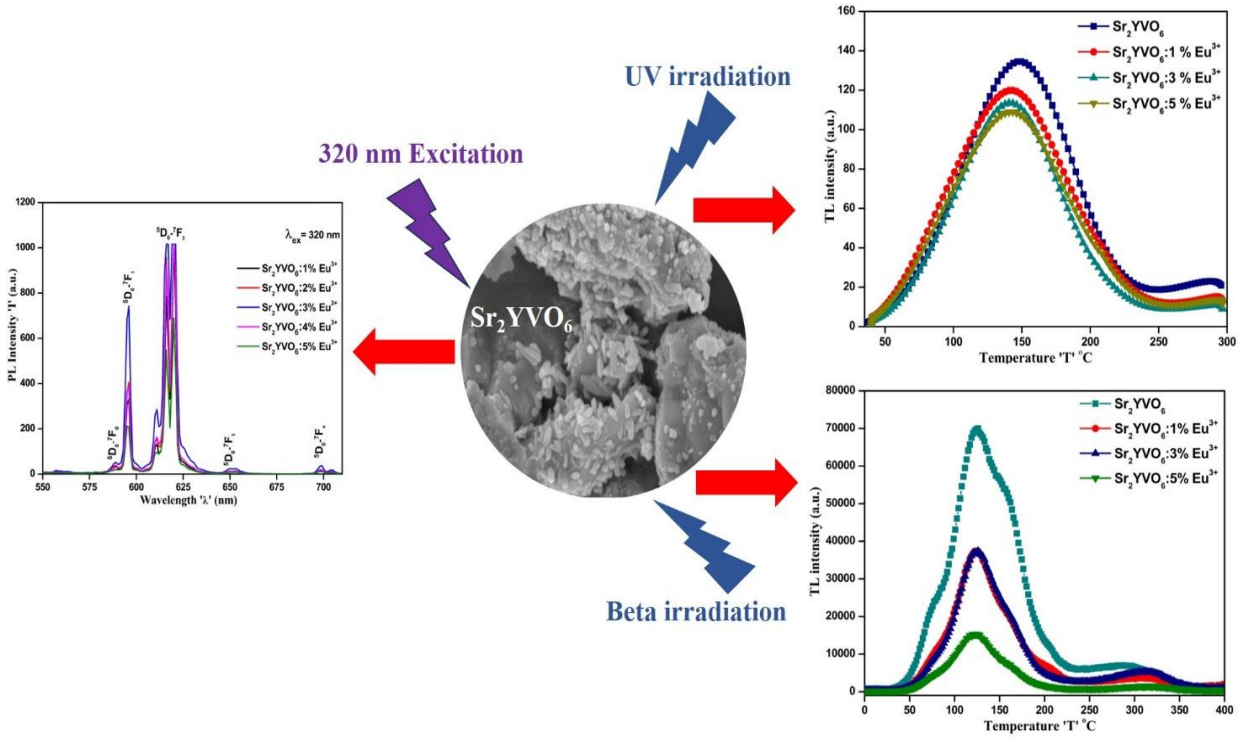

4.1 Introduction

The perovskite materials have gained significant attention due to their structural properties and potential applications in various fields of science and technology. Some of the key features of the perovskite materials make them very special to investigate, such as crystal structure, structural tunability, wide range of physical properties, ability to emit visible emission, and energy storage capacity. They continue to be a subject of intensive research due to their unique features for developments in various technological domains.

As per the literature survey, the double perovskite phosphors received less attention for their TL characterization; however, the PL in double perovskite was significantly studied. Besides perovskites, several papers have been published on the TL characterization of rare earth doped materials. The luminescent materials, such as $KMgF_3$: Tm [1], $K_2Ca_2(SO_4)_3$: Eu [2], $LiMgBO_3$:Dy^{3+} [3], LiF: Sm^{3+}/ Eu^{3+} [4], have been reported previously for their notable TL results after gamma irradiation. In addition, MgB_4O_7: Pr, Dy [5], $Ca_3Al_2O_6$ [6], Mg_2SiO_4:Eu^{3+} [7], ZrO_2:Er^{3+} [8] phosphors were extensively studied for their TL display after irradiating with beta radiation. Overall, comprehensive research has been carried out on the thermoluminescence of doped and undoped phosphors that have been irradiated with high-energy radiations, such as gamma rays, beta rays, X-rays, and shift heavy ions, which can produce deeper traps inside the phosphor materials. Moreover, as per the literature survey, a study on the TL of the phosphors that have been irradiated via UV radiation has also been reported previously. The comparatively lower-energy UV rays produce surface traps instead of deeper traps. Some examples of phosphors that show prominent TL display after UV irradiation include Gd_2O_3:Eu^{3+} [9], ZrO_2:Eu^{3+} [10], $SrMgAl_{10}O_{17}$: Eu [11], $La_2Zr_2O_7$: Gd [12]. With these references and the excellent PL display of the perovskites, it is motivating to explore the perovskites too for their TL characterization upon different ionizing radiation exposures.

In the present study, we reported the luminescence properties and practical applications of vanadate double perovskite Sr_2YVO_6 (SYV) as a host activated with Eu^{3+} for display devices and thermoluminescence dosimetry (TLD) using beta rays and UV rays. The synthesized series of Sr_2YVO_6:Eu^{3+} phosphor shows excellent red emission upon diverse excitations with extraordinary PL intensity. The influence of doping on luminescence optimization was investigated in detail. A highly intense PL intensity in the red spectral region with an additional far-red component was observed upon NUV excitation. Moreover, the thermoluminescence of the phosphor series was examined after irradiating with beta radiation and UV rays of 254 nm

(E = 4.88 eV) to assess the radiation dosimetry aspects. Obtained TL results revealed high sensitivity at minor doses, displaying a linear dose-response to the ionizing radiations.

4.2 Synthesis and Characterizations

4.2.1 Phosphor Preparation

Six samples of Sr_2YVO_6 double perovskites doped with Eu^{3+} were prepared, in which the Eu^{3+} doping level was taken from 1-5 mol%. For the phosphor synthesis, high-temperature combustion route was considered. The analytical reagent (AR) grade strontium nitrate ($Sr(NO_3)_2$, 99.5% pure), yttrium oxide (Y_2O_3, 99.9% pure), vanadium pentoxide (V_2O_5, 99.9% pure), and europium oxide (Eu_2O_3, 99.9% pure) of loba-chemical supplier are taken in stoichiometric proportions. These raw materials were carefully mixed with urea (15% weight of the entire mix, 99%) to achieve homogeneity. Urea was taken to initiate the combustion reaction within raw materials. All these raw materials were grounded first and calcinated at 1200°C for 6 hr in the muffle furnace. After heating treatment, all phosphors are allowed to natural cool up to room temperature. The resultant product looks like a foamy solid, and was then further grounded to get consistent white phosphor powder. All the samples under study were prepared at same conditions [13].

4.2.2 Characterizations

First, the phosphors under study were characterized for their XRD analysis for the structure formation and structural attributes. The XRD were recorded via a D8 Bruker advance X-ray diffractometer within 20° to 70° angle of diffraction with a step of 0.02°/s. To visualize the phosphor surface, the SEM characterization is carried out at different scanning resolutions, mainly 200 nm and 2 µm. The FTIR spectra were monitored via a Jasco FTIR-4100 spectrometer in transmittance mode, by using the KBr pellet technique. The PL spectra of all the phosphors under study were recorded using Shimadzu Spectro-fluorophotometer, wherein xenon flash lamp was used as the excitation source. Furthermore, the TL of all the phosphors were recorded after the irradiation by beta rays using ^{90}Sr beta source and UV rays of 254 nm wavelength. The TL measurements after beta irradiation was done by using a Risø TL/OSL reader DA 15 (Bøtter-Jensen et al., 2003) instrument, and the TL measurements after UV irradiation were done by using the NUCLEONIX TL READER of type TL1009 [13].

4.3 Results and Discussion

4.3.1 XRD Studies

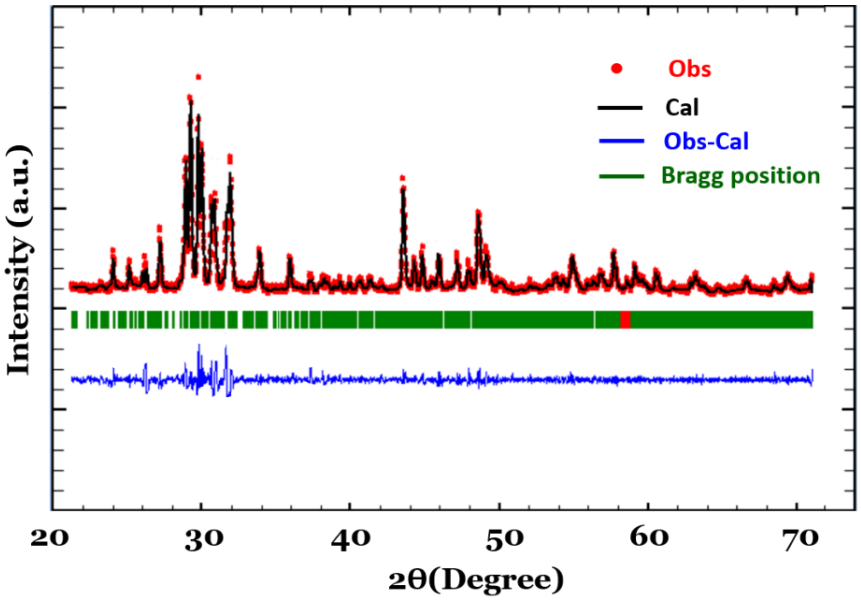

Figure 4.1. Rietveld refined XRD pattern of Sr_2YVO_6 phosphor.

In the present phosphor system, a structural investigation was conducted through Rietveld refinement using the Fullprof Suite, an extensively used computer software for the analysis of diffraction patterns. The refined diffraction pattern of the pure Sr_2YVO_6 phosphor is depicted in Figure 4.1. The obtained results from the structural refinement indicate that the material under study is crystalline in a pure monoclinic crystal structure. The reliable factors associated with the pattern fitting were obtained to be $R_p = 23.2\%$, $R_{pw} = 25.8\%$, and $\chi^2 = 3.04$. The cell parameters of the present double perovskite are a = 21.15 Å, b = 4.65 Å, c = 20.18 Å, $\beta = 91.54°$, and the cell volume V = 1986.94 $Å^3$. The vital diffraction peaks produced in the diffraction pattern were indexed to a monoclinic structure with a P_2/m space group [13,14].

Figure 4.2 depicts the diffraction patterns of base and Eu^{3+} activated double perovskite Sr_2YVO_6, in which the europium concentration was taken from 1-5 mol%. The XRD patterns of the studied compositions exhibit prominent similarities. A slight variation in peak intensity distribution within the XRD patterns might be due to the incorporation of Eu^{3+}. Apart from intensity distribution, no further notable change in the diffraction patterns of doped and undoped phosphors was observed. The observations from the XRD pattern strongly indicate that the doping ion europium has no significant impact on the crystal structure of the host lattice. Moreover, the nature of the XRD peaks highlighted the highly crystalline material. The lattice parameters and structural attributes obtained from the Rietveld refinement have been briefly presented in Table 4.1.

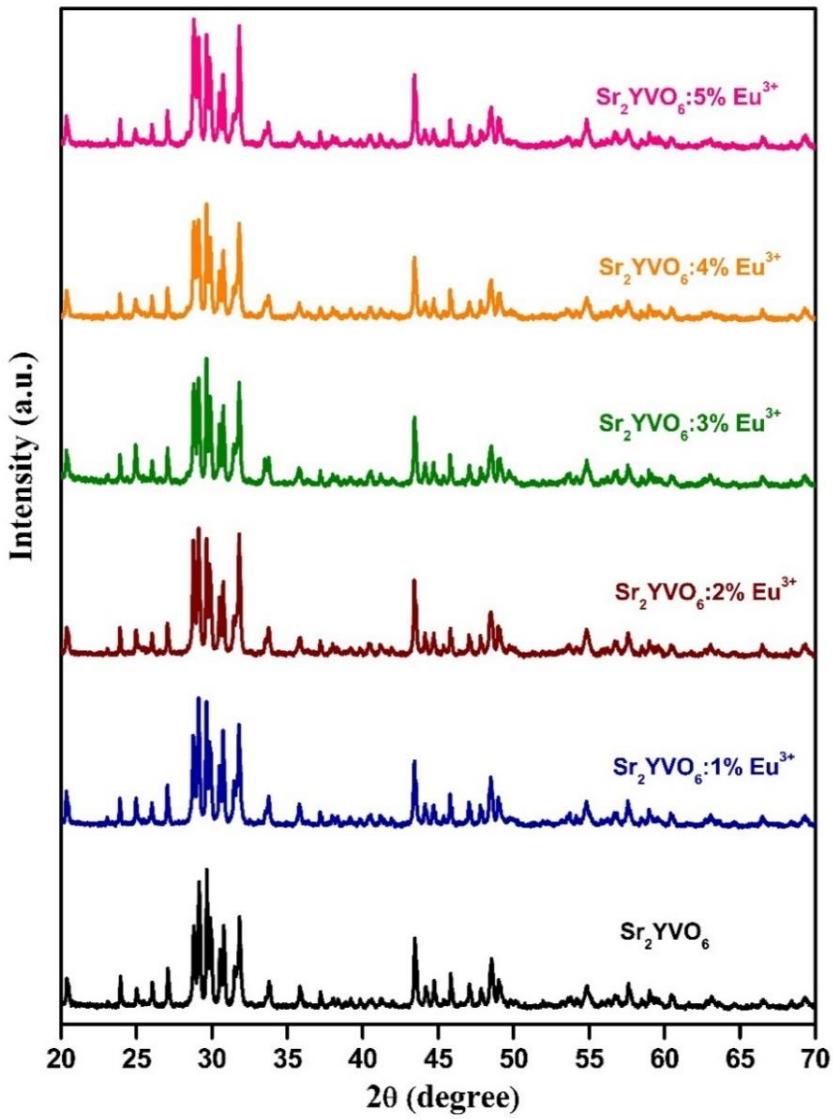

Figure 4.2. XRD patterns of Sr_2YVO_6: x mol% Eu^{3+} (x= 0-5) phosphors.

Samples	Lattice parameters				χ^2	Cell volume
	a (Å)	b (Å)	c (Å)	β		V (Å)
Sr_2YVO_6	21.15	4.65	20.18	91.54°	3.04	1986.94
Sr_2YVO_6:1% Eu^{3+}	21.17	4.65	20.19	91.59°	3.23	1989.98
Sr_2YVO_6:2% Eu^{3+}	21.17	4.65	20.19	91.60°	3.99	1988.87
Sr_2YVO_6:3% Eu^{3+}	21.18	4.65	20.19	91.59°	3.11	1987.68
Sr_2YVO_6:4% Eu^{3+}	21.18	4.65	20.21	91.60°	4.01	1989.64
Sr_2YVO_6:5% Eu^{3+}	21.18	4.65	20.11	91.60°	3.23	1989.44

Table 4.1. Summary of lattice parameters obtained through Rietveld refinement.

Furthermore, the tolerance factor is a crucial parameter used to assess the stability of a perovskite crystal structure. The tolerance factor is calculated using the ionic radii of the constituent cations in the phosphor and serves as an indicator of whether the chosen combination of cations can form a stable perovskite structure. Using formula 3.2, the tolerance factor is computed. The value of the tolerance factor can range from 0.77 to 1.0. The $T_f < 0.77$ suggests that the structure is distorted or non-cubic, such as orthorhombic or monoclinic, whereas $T_f \approx 1$ denotes ideal cubic perovskite. In the case of Sr_2YVO_6, the computed value of T_f equals 0.86, providing additional confirmation of the phosphor's monoclinic structure.

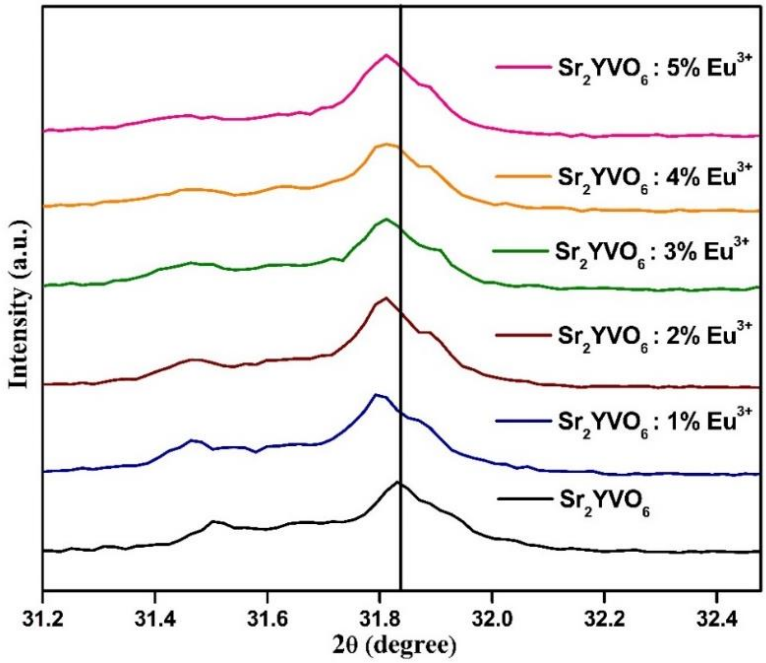

Figure 4.3. Magnified diffraction patterns of undoped and Eu^{3+} doped Sr_2YVO_6 phosphors.

As shown in Figure 4.2, the diffraction patterns of all the phosphors under investigation look closely similar. In order to identify the Eu^{3+} introduction, the most intense diffraction peak of the XRD patterns was magnified. Figure 4.3 depicts a magnified picture of the diffraction patterns of the phosphors under study. Upon magnification of the diffraction pattern, it is apparent that the most prominent diffraction peak of the XRD patterns in the doped samples has shifted towards a lower diffraction angle. This shift in the diffraction angle is gradual with increasing doping concentration. This phenomenon of shifting in diffraction angle can be ascribed to Vegard's law, according to which the introduction of a dopant does not result in the creation of an independent diffraction peak of its own but induces a notable shift in the host material's diffraction pattern [15]. The observed shifting in the diffraction angle of the host matrix's diffraction peak is a clear indication of dopant integration into the host matrix. The shift of the diffraction peak towards smaller 2θ can be attributed to the fact that the larger radius

cation Eu^{3+} (0.947 Å) takes the place of the smaller radius cation Y^{3+} (0.900 Å) within the host lattice.

In addition, due to the similar valence states and closely matched ionic radii of substituted and substituting ions, there is a solid probability that Eu^{3+} can effectively substitute Y^{3+} within the host matrix. The validation of site substitution can be confirmed by calculating the parameter called acceptance percentage difference, denoted as D_r. Formula 3.1 is utilized for the D_r calculation. For the $Sr_2YVO_6:Eu^{3+}$ phosphor, the computed Dr value was obtained to be 5.22%. This calculated D_r value verifies a greater probability of Eu^{3+} taking the place of Y^{3+} within the host structure [16].

The crystallite size calculation was accomplished by using the Debye-Scherer formulation and the W-H plot method, wherein equations 3.3 and 3.5 were used, respectively. By using the Debye-Scherer (D-S) formula for crystallite size calculation, the crystallite size of all the phosphors under study ranged from 50 nm to 62 nm.

Figure 4.4 (a) and (b) are the W-H plots of base and 1 mol% Eu^{3+} activated Sr_2YVO_6 phosphors. From the slope of the fitted straight line observed in the plot, the average crystallite size is calculated, whereas the intercept of the straight line itself denotes the micro-strain. From the W-H plot reading, the negative observed negative slope indicates the compressive strain of the phosphors. The computed crystallite size of all phosphors under study using this method ranged between 72 and 78 nm. The results obtained from the W-H plot analysis and Debye-Scherer (D-S) formula are tabulated in Table 4.2.

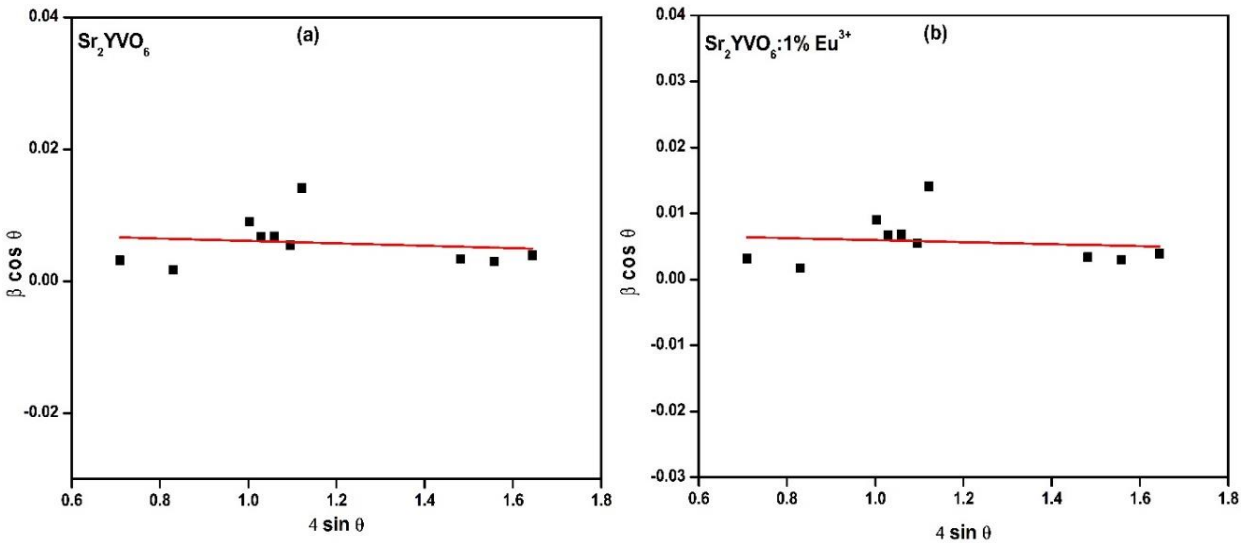

Figure 4.4. W-H plots of Sr_2YVO_6 (a) and Sr_2YVO_6:1% Eu^{3+} (b).

Sample	Crystallite size (nm)		Strain (ε)
	W-H Plot	D-S Formula	
Pure	72.40	52.18	7.92×10^{-3}
Sr_2YVO_6:1% Eu^{3+}	76.23	58.74	9.66×10^{-3}
Sr_2YVO_6:2% Eu^{3+}	74.45	55.63	2.45×10^{-3}
Sr_2YVO_6:3% Eu^{3+}	72.12	50.78	1.91×10^{-3}
Sr_2YVO_6:4% Eu^{3+}	77.87	61.05	9.87×10^{-3}
Sr_2YVO_6:5% Eu^{3+}	76.34	60.73	7.88×10^{-3}

Table 4.2. Crystallite size of Sr_2YVO_6 phosphors calculated using D-S and W-H methods.

4.3.2 SEM Studies

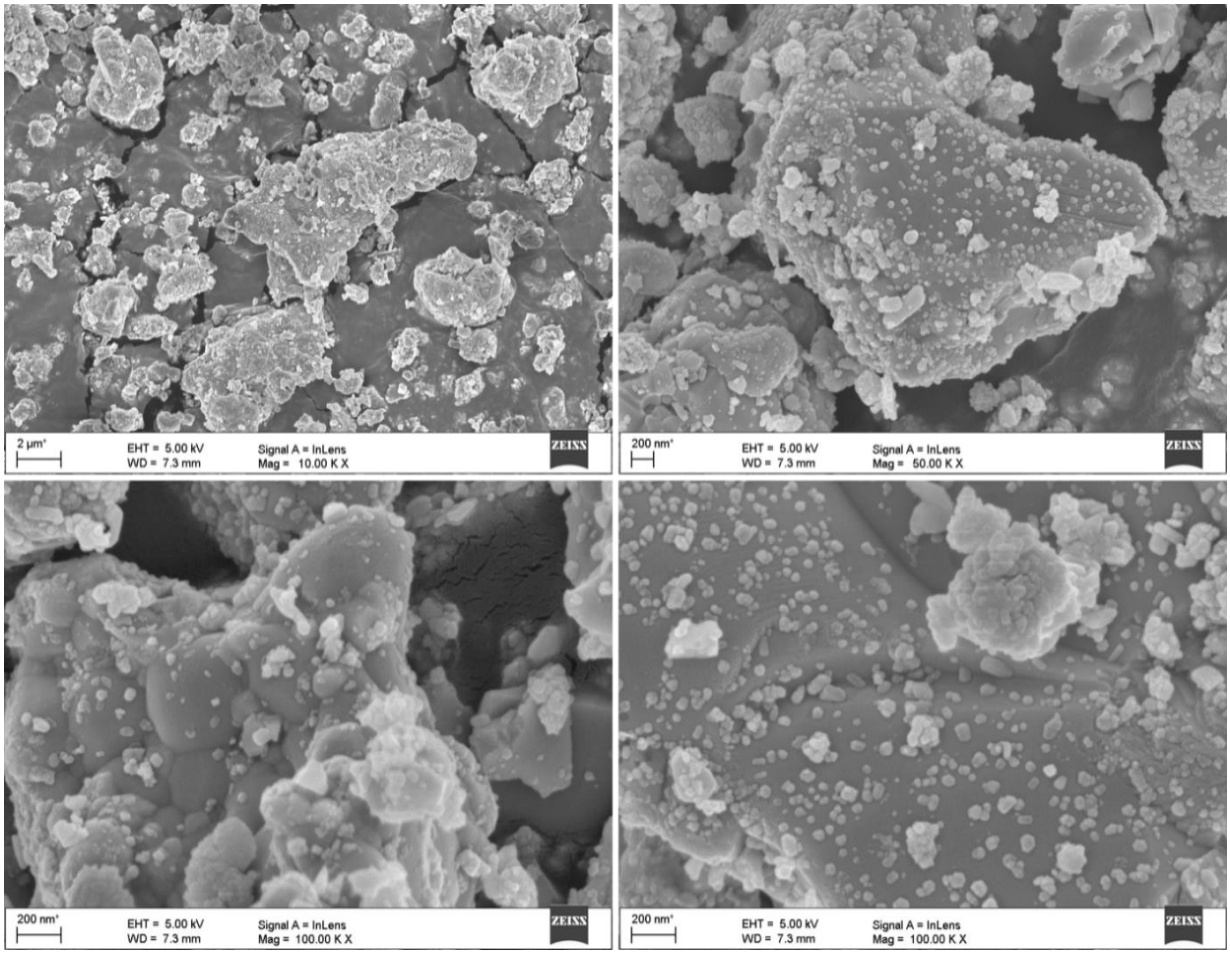

Figure 4.5. SEM micrographs of 3% Eu^{3+} doped Sr_2YVO_6 phosphor.

SEM is a powerful imaging technique used to visualize the surface morphology and topography of materials at very high resolution. Taking this into account, the SEM analysis was conducted to explore the surface characteristics of the as-synthesized Sr_2YVO_6:3%Eu^{3+}

phosphor. The results are depicted in Figure 4.5. The different scanning resolutions are used to study the surface of the phosphor. The SEM micrographs with scanning resolutions of 200 nm and 2 µm are depicted in Figure 4.5 (a-d). The SEM results exhibited a high degree of agglomeration with non-uniform shapes of the phosphor grains. The majority of the particles are distributed within the range of 100 nm to a micrometre.

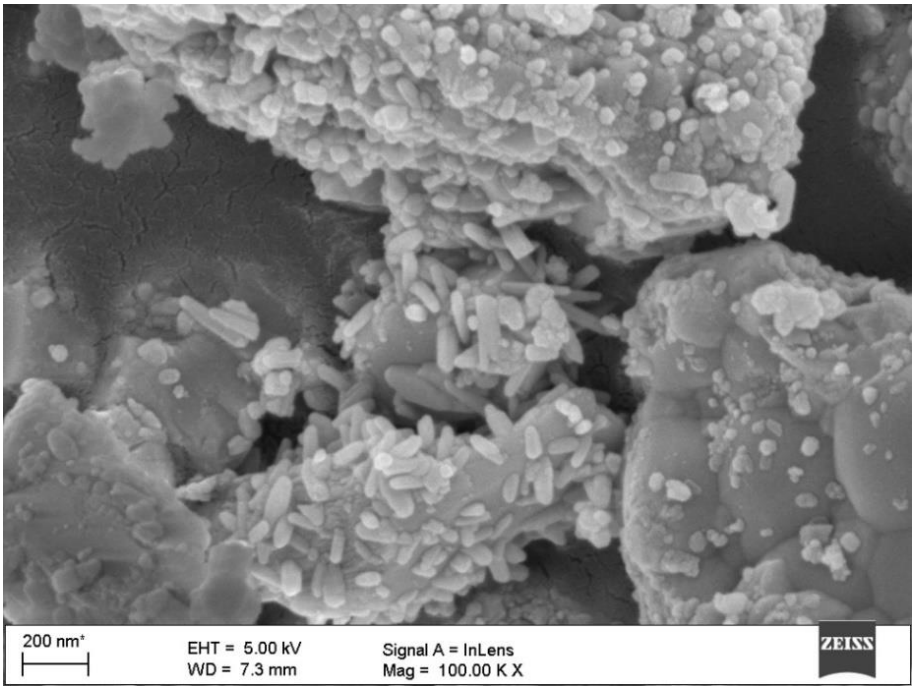

Figure 4.6. SEM micrographs of 3% Eu^{3+} doped Sr_2YVO_6 phosphor at scanning resolution of 200 nm.

However, evenly distributed nanorods, like rice seed shapes, were detected, and appeared as clusters, as shown in figure 4.6. The morphology reveals a porous surface, which is likely to be formed due to escaping gases during the combustion [17]. Moreover, high-temperature sintering can also be the cause of the irregular surface morphology. In summary, a micro-nano grain with a size of a few nanometres to a micrometre is seen.

4.3.3 EDAX Studies

EDAX is basically a surface analysis technique which is widely used in materials science to determine the elemental composition of various types of synthesized materials. EDAX analysis is an important tool applied for identifying elements in material mixture. Herein, the phosphor Sr_2YVO_6:3%Eu^{3+} underwent the EDAX study, shown in Figure 4.7. As shown in the spectra, the sample exhibits distinct peaks corresponding to each constituent element Sr, Y, V, O, and dopant Eu. The obtained EDAX results confirm the successful incorporation of Eu^{3+} ions into the host matrix.

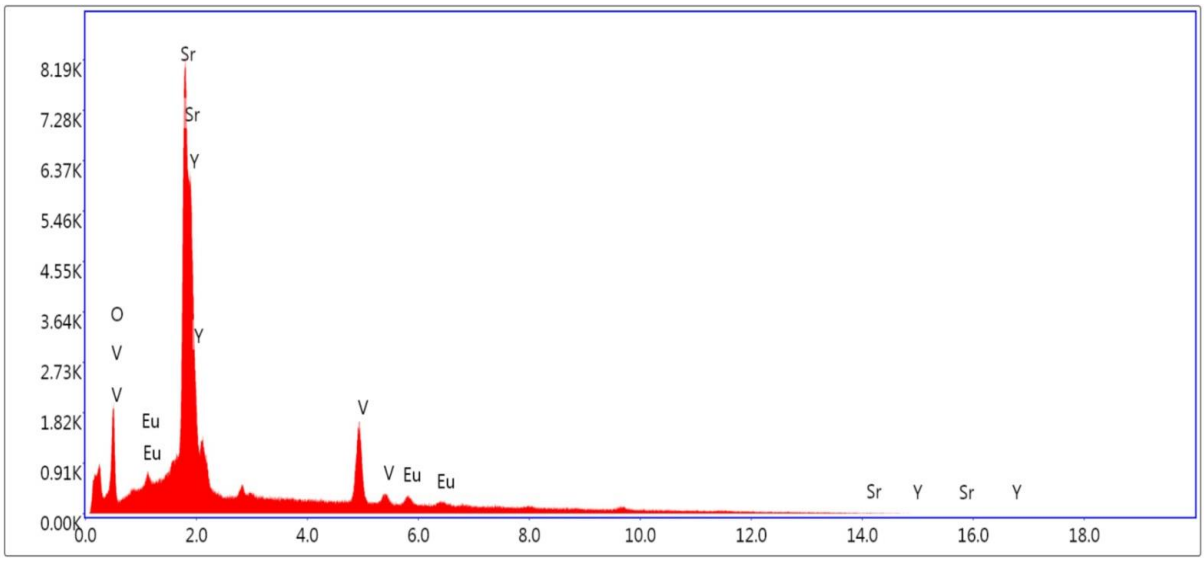

Figure 4.7. EDAX of 3 mol% Eu^{3+} doped Sr_2YVO_6 phosphor.

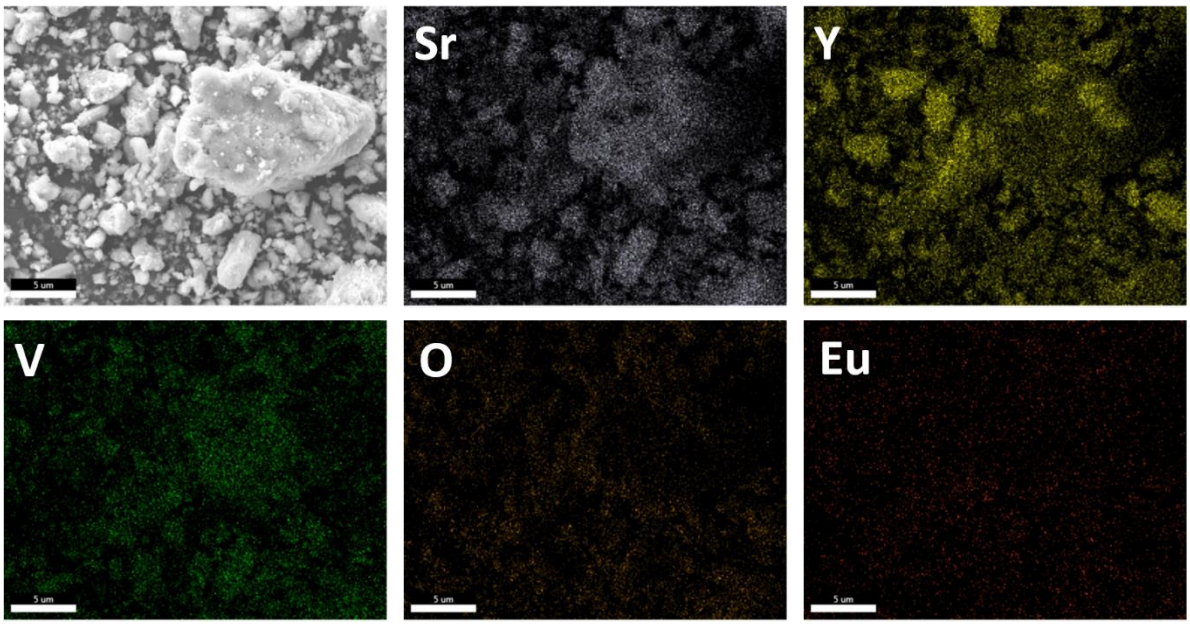

Figure 4.8. Elemental mapping of 3% Eu^{3+} doped Sr_2YVO_6.

Moreover, the elemental distribution was represented in Figure 4.8. In the mapping pictures of Sr_2YVO_6:3%Eu^{3+}, the presence of the constituent elements, namely Sr, Y, V, O, and Eu, is clearly visible in separate color-coded images. These elemental maps reveal a homogeneous dispersion of all constituent elements within the material. Apart from the host matrix elements, a minimally incorporated Eu^{3+} dopant also looks evenly distributed through the material. This is due to the proper grinding of the raw materials before sintering.

4.3.4 FTIR Studies

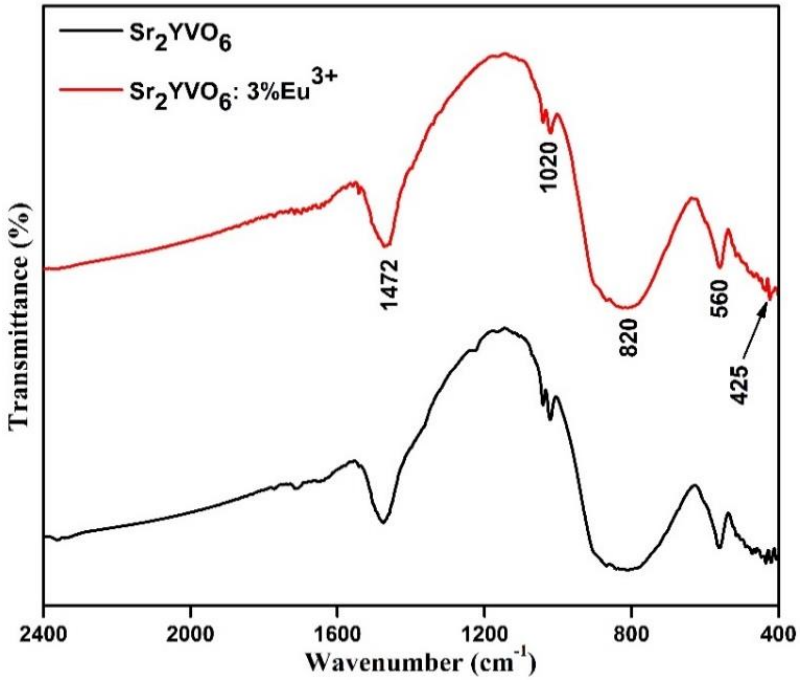

Figure 4.9. FTIR spectra of undoped and 3 mol% Eu^{3+} doped Sr_2YVO_6 phosphors.

Figure 4.9 depicts the FTIR spectra of both the pristine and 3 mol% Eu^{3+} activated Sr_2YVO_6 phosphors, covering 400 cm^{-1} to 2400 cm^{-1} of wavenumber region. To obtain these spectra, a KBr pellet method was employed. A nearly similar spectra were recorded for both materials mentioned. In the spectrum, a small absorption hump at 425 cm^{-1} described the bending vibration of the O-Sr-O bond within the phosphor [18]. The Y-O metal-oxide bond's distinctive peaks were identified at roughly 560 cm^{-1} and 1020 cm^{-1}, signifying the Y-O stretching vibration mode [19]. The symmetric stretching vibration of existing VO_6 octahedra was attributed to a broad band at approximately 820 cm^{-1}, while the other V-O vibration mode within the phosphor was represented by another wide band at 1472 cm^{-1} [14]. The FTIR study results gave sufficient confirmation of the presence of standard functional groups.

4.3.5 Photoluminescence Studies

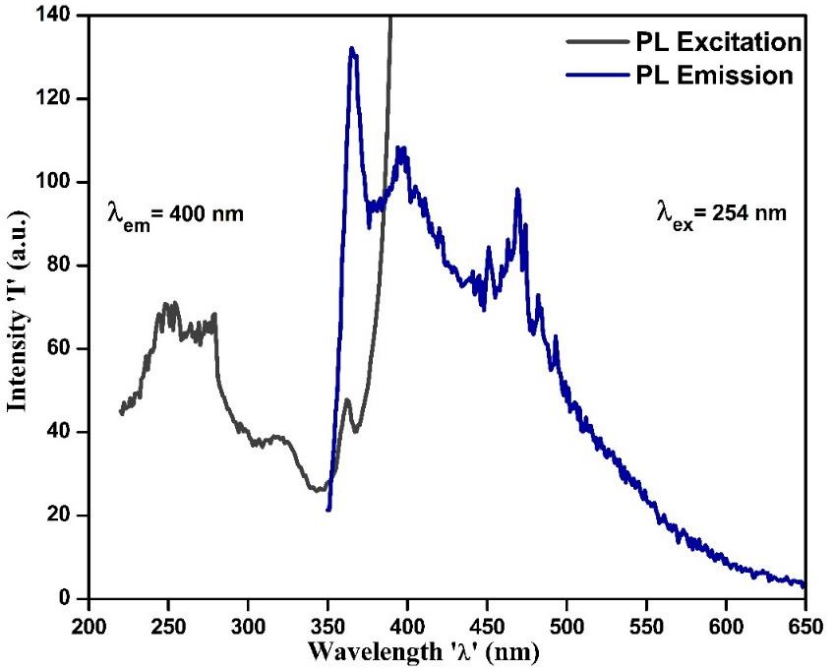

Figure 4.10. Photoluminescence excitation and emission spectra of pure Sr_2YVO_6.

Figure 4.10 depicts the PL excitation and PL emission spectrum of the host lattice. A weakly intense excitation peak at around 254 nm is observed. When the host material is excited at 254 nm, a sharp emission peak is observed at 475 nm, along with the material crystal field towards the shorter wavelength side. The emission peak detected at 475 nm can be attributed to host matrix emission in the principle of Y^{3+} cation.

Figure 4.11 (a) and (b) depict the PL excitation spectrum and PL emission spectra of 1 mol % Eu^{3+} doped Sr_2YVO_6 phosphor, respectively. The PL excitation spectrum was monitored at 612 nm at RT. The excitation spectrum was obtained within the 220-500 nm wavelength. When the phosphor is monitored with 612 nm, several excitation peaks have been observed, primarily at 278, 320, 396 and 467 nm. These excitation peaks are ascribed to different charge transfer (CT) processes and a standard electronic transition occurring due to different electronic states of the luminescent activator Eu^{3+}. The excitation region between 220-350 nm reveals two distinct absorption bands at 278 nm and 320 nm.

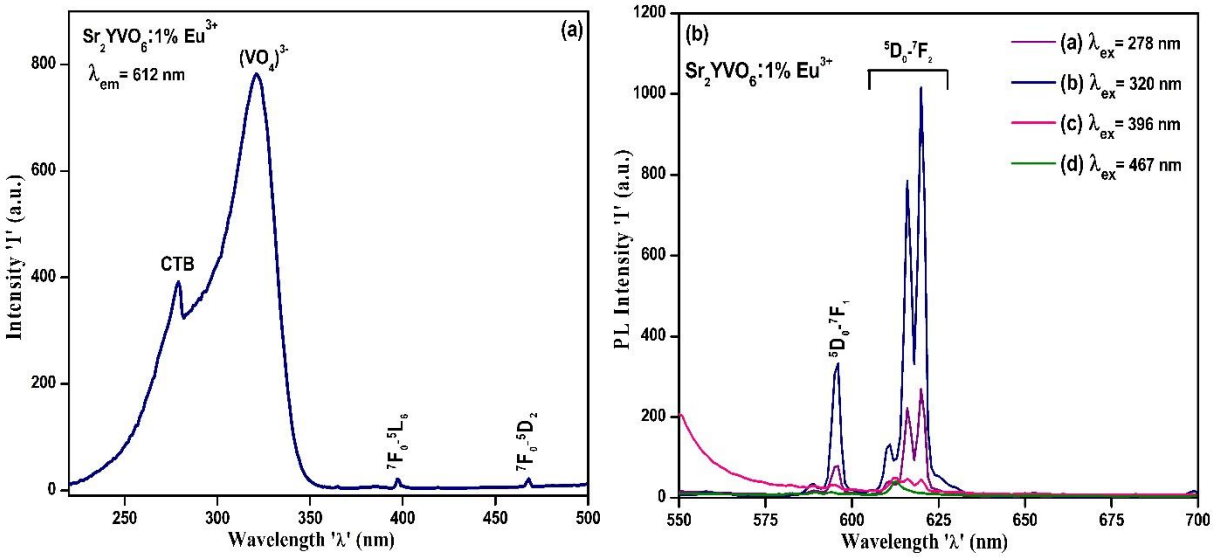

Figure 4.11. PL excitation (a) and PL emission (b) spectra of Sr_2YVO_6: 1 mol% Eu^{3+} phosphor.

These district bands were arisen due to the CT processes. The sharp-edged band cantered at 278 nm was assigned to the CT process between the 2p orbital of O^{2-} and the 4f orbital of Eu^{3+} [20-22]. Whereas, a well-resolved absorption band cantered at 320 nm is ascribed to the CT absorption of the tetrahedrally coordinated $(VO_4)^{3-}$ group [23]. From the figure, it is observed that the broad absorption band cantered at 320 exhibited maximum intensity when compared to all other excitation peaks identified. This indicates that the intensity is due to the absorption of the vanadate group dominating the excitation spectrum. In this absorption region (220-350 nm), the lower energy charge transfer absorption at 320 nm (3.87 eV) was observed due to the presence of Sr^{2+} and Y^{3+} ions in the host matrix, which have larger ionic radii and lower valance states compared to V^{5+} [24]. Furthermore, the PL excitations due to intra-4f transitions of Eu^{3+} were observed at 396 nm and 467 nm, which are attributed to $^7F_0$-$^5L_6$ and $^7F_0$-$^5D_2$ transitions, respectively. Moreover, the other europium excitations with very low intensities were also detected at 365, 385, and 420 nm, which are ascribed to $^7F_0$-$^5D_4$, $^7F_0$-$^5L_7$, and $^7F_0$-$^5D_3$ typical Eu^{3+} transitions, respectively [25-28].

The PL emission from Sr_2YVO_6:1 mol% Eu^{3+} phosphor was recorded by applying 278, 320, 396, and 467 nm excitations. The spectra were obtained at ambient temperature within the wavelength range of 550-700 nm, and the results are illustrated in Figure 4.11 (b). A closely identical pattern of PL emission was observed under both 278 nm and 320 nm excitations, in which the intensity due to the excitation of 320 nm is maximum. The PL emission that appeared in the orange-red spectral region is observed collectively due to the MD transition $^5D_0$-$^7F_1$ and ED transition $^5D_0$-$^7F_2$ of doping ions. When the phosphor was excited with 278 nm and 320 nm

excitations, $^5D_0$-$^7F_0$ (at 580 nm), $^5D_0$-$^7F_1$ (at 596 nm), and $^5D_0$-$^7F_2$ (at 611, 616, and 620 nm) transitions of Eu^{3+} were detected with dominating red emission at 620 nm [29-31]. Moreover, under the excitation of 396 nm and 467 nm, a similar transition of Eu^{3+} was detected with poor peak intensity. An excellent PL display of Sr_2YVO_6: Eu^{3+} phosphor under UV (278 nm) and NUV (320 nm) excitation makes it very special to be used in display devices as a red-emitting component. Table 4.3 displays the intensity counts of PL excitation and subsequent emission counts of 1 mol% Eu^{3+} doped Sr_2YVO_6 phosphor.

Ex Peak		**278 (nm) (E= 4.52 eV)**	**320 (nm) (E= 3.87 eV)**	**396 (nm) (E= 3.13 eV)**	**467 (nm) (E= 2.65 eV)**
Ex Intensity		391	776	21	22
Emission	**Emission Peak (nm)**	**Emission Intensity**	**Emission Intensity**	**Emission Intensity**	**Emission Intensity**
	596	78	331	32	13
	611	37	132	50	37
	616	221	785	46	-
	620	270	1015	45	12

Table 4.3. PL intensities of various excitation and emission peaks of 1 mol% Eu^{3+} doped Sr_2YVO_6 phosphor.

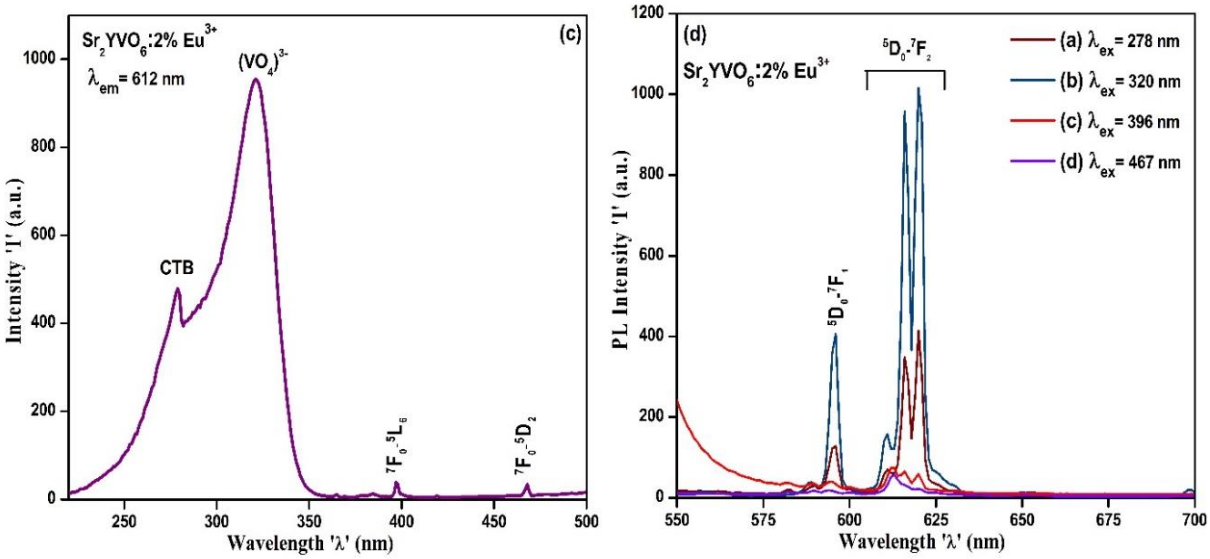

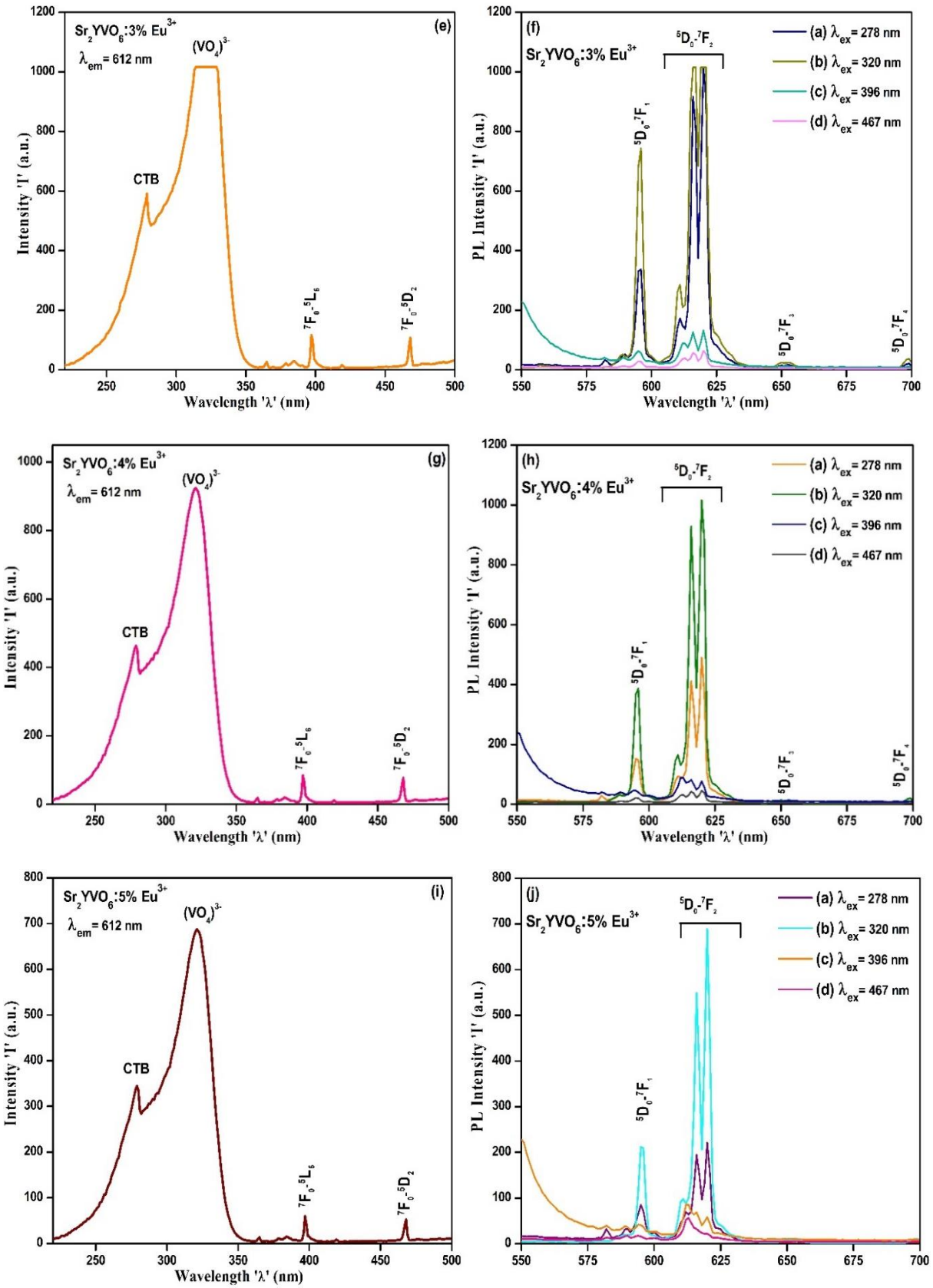

Figure 4.11. (c) PL excitation and (d) PL emission spectra of Sr_2YVO_6:2 mol% Eu^{3+} phosphor; (e) PL excitation and (f) PL emission spectra of Sr_2YVO_6:3 mol% Eu^{3+} phosphor; (g) PL excitation and (h) PL emission spectra of Sr_2YVO_6:4 mol% Eu^{3+} phosphor; (i) PL excitation and (j) PL emission spectra of Sr_2YVO_6:5 mol% Eu^{3+} phosphor.

Figure 4.11 (c-j) depicts the PL excitation and respective PL emission spectra of the Sr_2YVO_6:x mol% Eu^{3+} (x = 2-5) phosphors. From the figure, it is observed that all the phosphors with various Eu^{3+} concentrations exhibited a similar pattern of PL excitation and PL emission, in which the phosphor containing 3 mol% of Eu^{3+} displays the highest PL intensity. In addition, interesting far-red emission peaks are observed at 653 nm and 705 nm from the phosphor doped with 3 mol% of Eu^{3+} when it is excited at 278 nm and 320 nm excitations. These far-red components of PL emission at 653 nm and 705 nm are ascribed to the ED transitions $^5D_0$-$^7F_3$ and $^5D_0$-$^7F_4$ of Eu^{3+}, respectively [32,33]. It is worth mentioning here that the existence of far-red component upon NUV (320 nm) excitation suggests that the 3 mol % Eu^{3+} activated phosphor under study may also be used for plant growth purposes.

Ex Peak		**278 (nm) (E= 4.52 eV)**	**320 (nm) (E= 3.87 eV)**	**396 (nm) (E= 3.13 eV)**	**467 (nm) (E= 2.65 eV)**
Ex Intensity		478	955	39	33
Emission	**Emission Peak (nm)**	**Emission Intensity**	**Emission Intensity**	**Emission Intensity**	**Emission Intensity**
	596	128	406	40	18
	611	70	158	73	51
	616	348	957	64	-
	620	413	1015	58	20

Table 4.4. PL intensities of various excitation and emission peaks of 2 mol% Eu^{3+} doped Sr_2YVO_6 phosphor.

Ex Peak		**278 (nm) (E= 4.52 eV)**	**320 (nm) (E= 3.87 eV)**	**396 (nm) (E= 3.13 eV)**	**467 (nm) (E= 2.65 eV)**
Ex Intensity		590	1015	116	107
Emission	**Emission Peak (nm)**	**Emission Intensity**	**Emission Intensity**	**Emission Intensity**	**Emission Intensity**
	596	336	742	62	29
	611	172	285	90	36
	616	916	1016	126	56
	620	1016	1016	131	63

Table 4.5. PL intensities of various excitation and emission peaks of 3 mol% Eu^{3+} doped Sr_2YVO_6 phosphor.

Ex Peak		**278 (nm) (E= 4.52 eV)**	**320 (nm) (E= 3.87 eV)**	**396 (nm) (E= 3.13 eV)**	**467 (nm) (E= 2.65 eV)**
Ex Intensity		463	924	85	78
Emission	**Emission Peak (nm)**	**Emission Intensity**	**Emission Intensity**	**Emission Intensity**	**Emission Intensity**
	596	151	386	46	21
	611	94	164	88	29
	616	411	928	81	42
	620	490	1015	76	45

Table 4.6. PL intensities of various excitation and emission peaks of 4 mol% Eu^{3+} doped Sr_2YVO_6 phosphor.

Ex Peak		**278 (nm) (E= 4.52 eV)**	**320 (nm) (E= 3.87 eV)**	**396 (nm) (E= 3.13 eV)**	**467 (nm) (E= 2.65 eV)**
Ex Intensity		344	682	60	52
Emission	**Emission Peak (nm)**	**Emission Intensity**	**Emission Intensity**	**Emission Intensity**	**Emission Intensity**
	596	85	212	41	18
	611	70	92	85	56
	616	194	549	68	-
	620	221	688	57	22

Table 4.7. PL intensities of various excitation and emission peaks of 5 mol% Eu^{3+} doped Sr_2YVO_6 phosphor.

Tables 4.4, 4.5, 4.6, and 4.7 show the PL excitation and PL emission intensity counts of 2, 3, 4, and 5 mol% Eu^{3+} doped Sr_2YVO_6 phosphors, respectively. Among all the phosphors under study, the phosphor containing 3 mol% of Eu^{3+} exhibited excellent PL response.

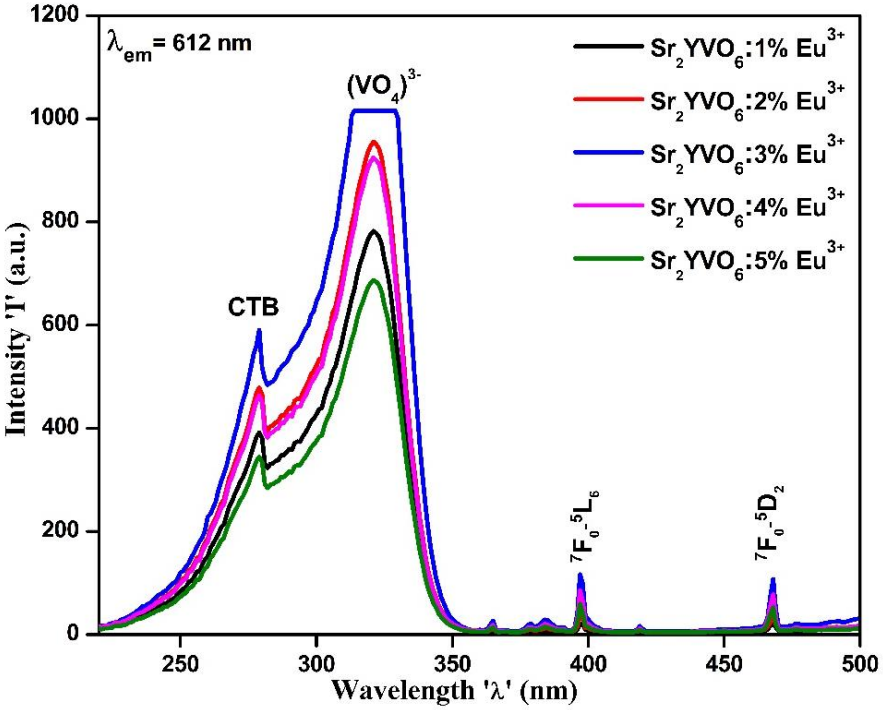

Figure 4.12. Photoluminescence excitation spectra of Sr_2YVO_6: x mol% Eu^{3+} (x =1-5) phosphors.

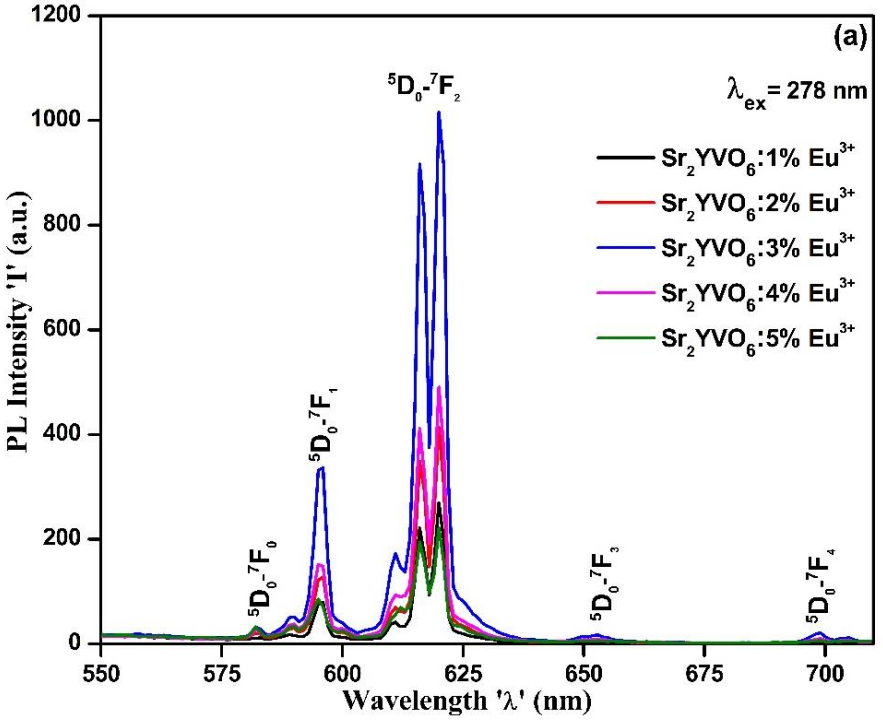

Figure 4.13. (a) PL emission spectra of Sr_2YVO_6: x mol% Eu^{3+} (x =1-5) phosphors monitored with 278 nm excitation wavelength.

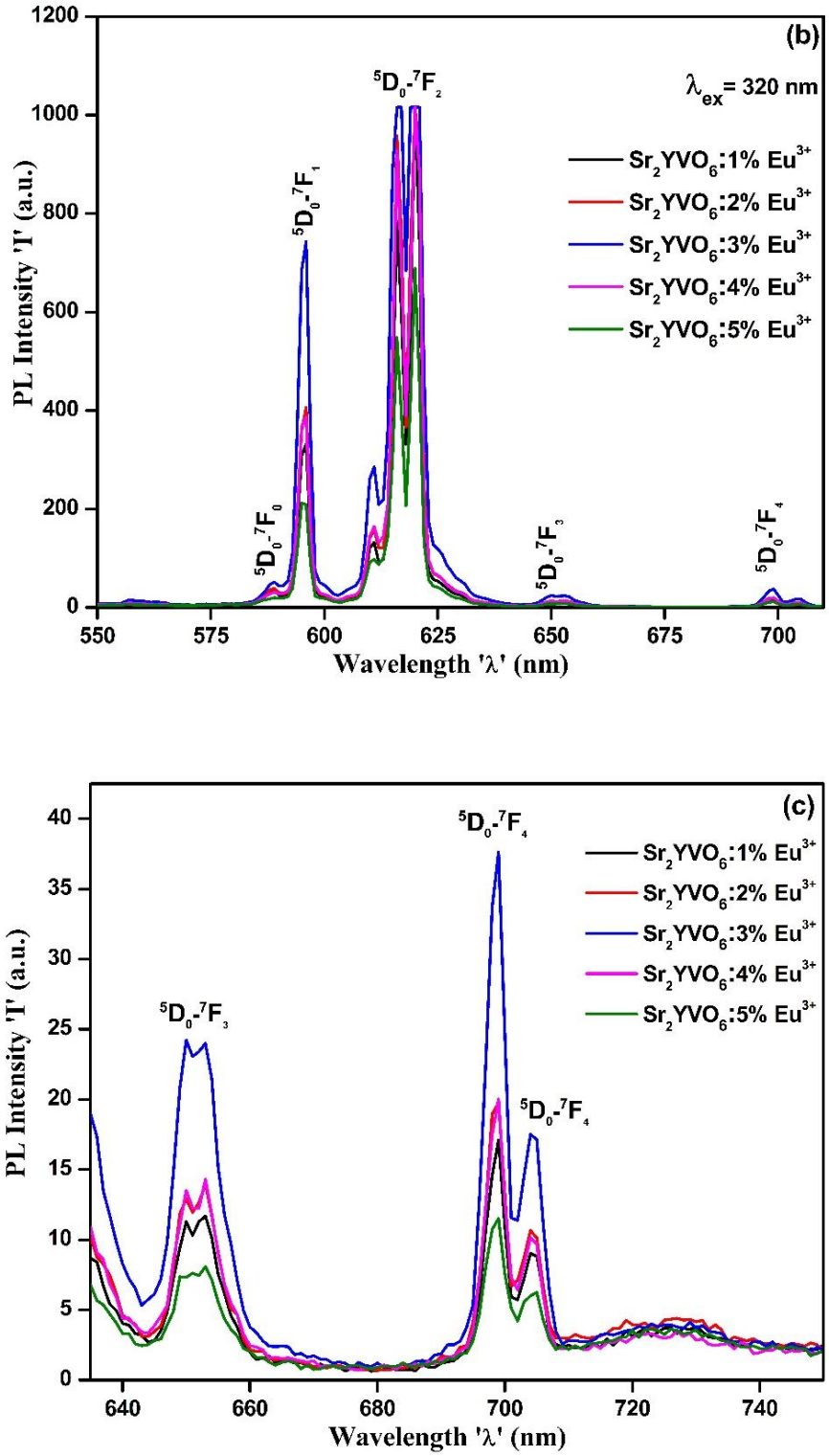

Figure 4.13. (b) PL emission spectra of Sr_2YVO_6: x mol% Eu^{3+} (x =1-5) phosphors monitored with 320 nm excitation wavelength; and (c) Magnified image of PL emission spectra of Sr_2YVO_6: x mol% Eu^{3+} phosphors within 630-750 nm.

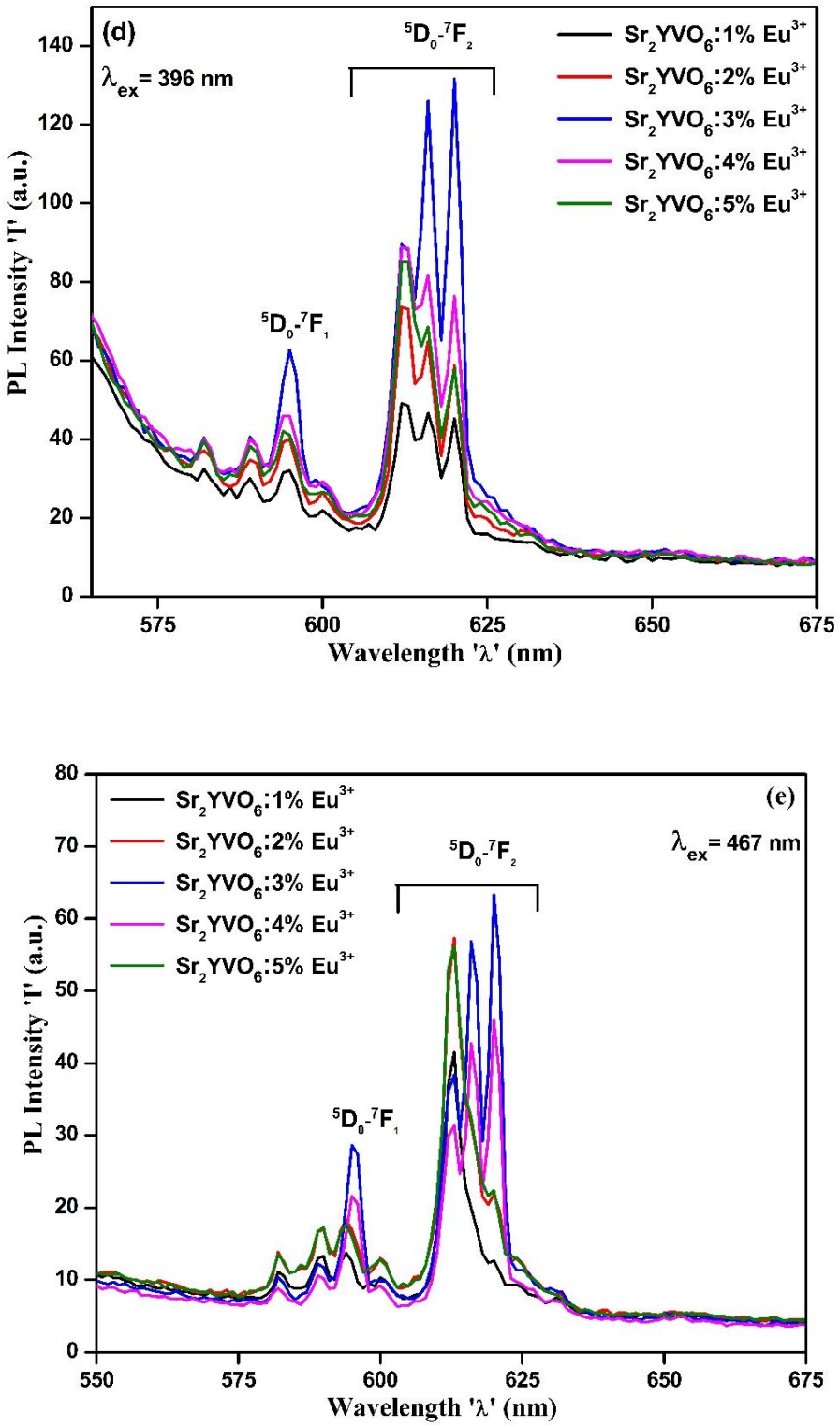

Figure 4.13. (d) PL emission spectra of Sr_2YVO_6: x mol% Eu^{3+} (x =1-5) phosphors monitored with 396 nm; and (e) PL emission spectra of Sr_2YVO_6: x mol% Eu^{3+} (x =1-5) phosphors monitored with 467 nm excitation wavelength.

Figure 4.12 depicts the combined graphs of the PL excitation spectra from Eu^{3+} activated Sr_2YVO_6:Eu^{3+} phosphors, wherein, the Eu^{3+} doping was increasing from 1 to 5 mol%.

The excitation spectra were monitored with 612 nm emission. Figure 4.13 (a) and (b) depict the combined graph of PL emission spectra of Sr_2YVO_6: Eu^{3+} phosphors recorded with 278 nm and 320 nm excitations, respectively. The enlarged image of emission spectra of Sr_2YVO_6:x mol% Eu^{3+} (x =1-5) phosphors under 320 nm excitation covering the 625-750 nm wavelength region was separately given in order to visualize the far-red PL emission, shown in Figure 4.13 (c). Figure 4.12 (d) and (e) are the combined graphs of the PL emission spectra of all phosphors under study recorded with 396 and 467 nm, respectively.

From the combined graphs of PL excitation and PL emission, as well as from Tables 4.3, 4.4, 4.5, 4.6, and 4.7, it is found, that when the phosphors under study were excited at 278, 320, 396 and 467 nm, the highest PL peak intensity was obtained from the phosphor containing 3 mol% Eu^{3+} concentration.

The dominance of PL intensity resulting from the electric dipole (ED) transition $^5D_0$-$^7F_2$ is evidently observable within the emission spectrum when compared to the MD transition $^5D_0$-$^7F_1$. In addition, the ED transition, often referred to as a hypersensitive transition, shows high sensitivity to its surrounding environment, and the intensity of PL due to the ED transition is strongly influenced by its surroundings. On the other hand, the $^5D_0$-$^7F_1$ magnetic dipole transition was less affected by the surrounding environment [34,35]. As per the Judd-Ofelt theory, the intensity dominance due to ED $^5D_0$-$^7F_2$ transition specifies the site occupancy of doping ions at a non-inversion centre within the host matrix. Particularly in the case of Eu^{3+} ions, it is well established that when Eu^{3+} occupies a non-centro symmetry site within the host lattice, the MD $^5D_0$-$^7F_1$ transition remains parity forbidden, while the ED $^5D_0$-$^7F_2$ transition is parity allowed. However, in the case of where Eu^{3+} ions are situated within an inversion symmetry, the emissions resulting from the $^5D_0$-$^7F_1$ MD transition were predominant. Furthermore, a supporting factor R (Asymmetry ratio) was computed for further identification of doping site symmetry. It is denoted as I($^5D_0$-$^7F_2$)/I($^5D_0$-$^7F_1$), and was used to confirm the asymmetry of the Eu^{3+} ion's location. Where I($^5D_0$-$^7F_2$) denotes the intensity of the hypersensitive transition of Eu^{3+}, whereas I($^5D_0$-$^7F_1$) stands for the intensity of MD transition $^5D_0$-$^7F_1$. A significantly high value of the asymmetry ratio, ranging between 1.35 and 2.40 (greater than unity), provides solid indication of the placement of the Eu^{3+} at a non-symmetrical site within the base material [36,37].

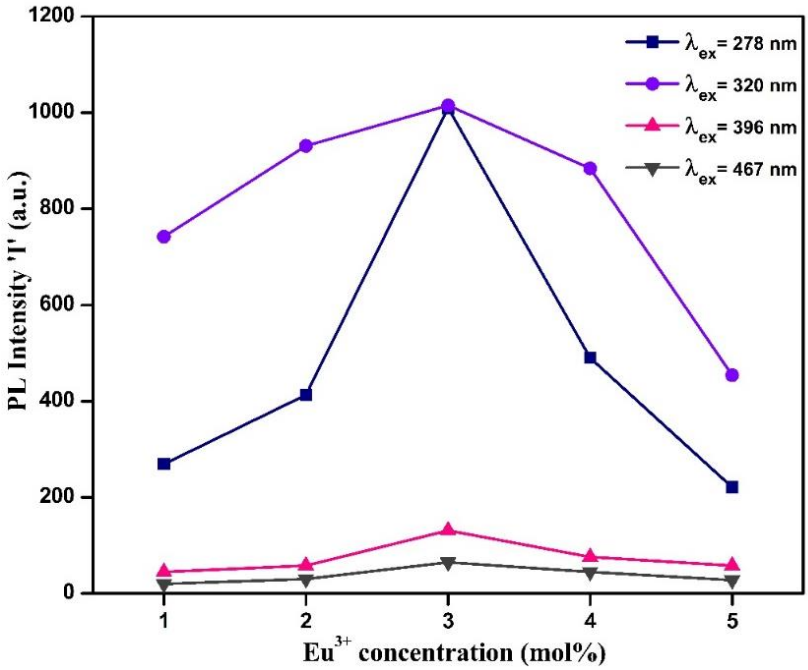

Figure 4.14. Plot of PL intensity as a function doping concentration.

From the combined graphs, it is seen, that as the Eu^{3+} doping level is increased, a substantial rise in the photoluminescence emission intensity in the red spectral region was observed. Whereas, the nature of the emission spectrum remained unaffected. The highest PL emission intensity was achieved when the phosphor contained 3 mol% of Eu^{3+}. Figure 4.14 illustrates the relationship amongst PL intensity and the Eu^{3+} concentration. From the figure, it is observed that the intensity of PL emission was increased when the doping level was raised from 1 to 3 mol%. [38]. Further increments in doping level result in the phenomenon of concentration quenching. Upon 4 mol% of Eu^{3+} doping, the intensity of PL emission is reduced by 10 % in the case of 320 nm excitation, whereas, 50 % reduction in PL intensity is observed in the case of 278 nm excitation. As the concentration of europium increases, the space between adjacent Eu^{3+} ions decrease. Consequently, this reduction in distance leads to non-radiative energy transfer between neighbouring doping ions, which then results in intensity quenching. Concentration quenching occurs when the doping level exceeds a specific threshold. The phenomenon of concentration quenching is induced either by multipole-multipole interaction or by exchange interactions, which can be confirmed through the calculation of a critical distance between adjacent activators [39]. The critical distance was denoted as R_c and was computed using the formula 3.6. The calculated value for R_c was 36 Å (>5 Å), which strongly indicated the multipolar interaction is the cause of concentration quenching [40]. Exchange interaction did not play any role in the photoluminescence intensity quenching process.

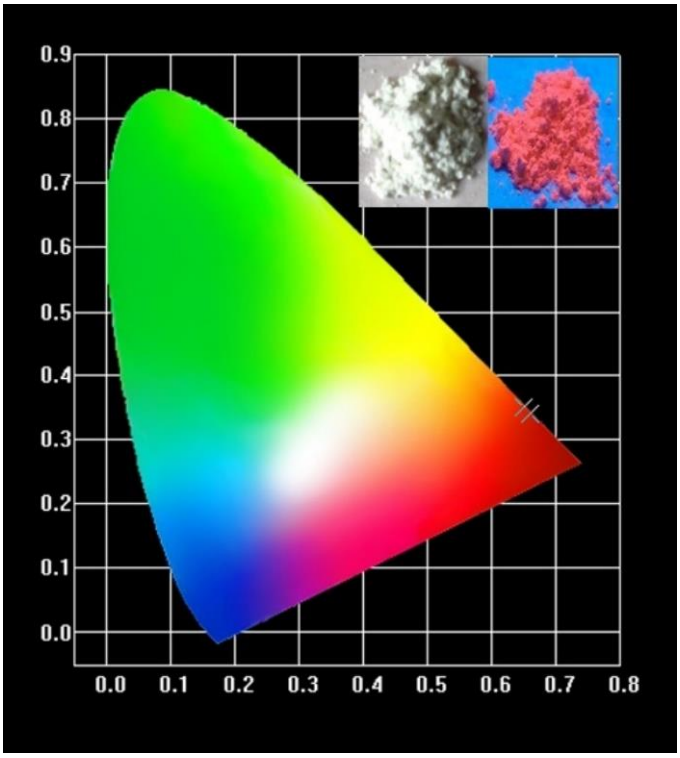

Figure 4.15. CIE diagram of Sr_2YVO_6:3 mol% Eu^{3+} phosphor.

In order to examine the color performance and the color purity, the study on CIE color coordinates was carried out for all the $Sr_2YVO_6:Eu^{3+}$ phosphors under study. Figure 4.15 depicts the CIE points of 3 mol% Eu^{3+} containing Sr_2YVO_6 phosphor. The calculated color coordinates of Sr_2YVO_6 phosphor doped with 3 mol% of Eu^{3+} are obtained to be (0.603, 0.387) for the excitation of 278 nm. However, for 320, 396 and 467 nm excitations, the computed color coordinates are (0.637, 0.360), (0.494, 0.504), and (0.456, 0.504), respectively. The computed values of the color coordinates found to be nearly equals to the typical red coordinates. Furthermore, the identification of far-red component in the studied phosphor system is verified [41,42].

In addition, the color purity of all the $Sr_2YVO_6:Eu^{3+}$ phosphor under study is determined. Under all the applied excitations, the color purity of Sr_2YVO_6:3%Eu^{3+} phosphor was quite good, which indicates that the studied phosphor system is promising for its application in lighting displays.

Moreover, the CCT was also computed using the McCamy method, wherein the CIE color coordinates were utilized. The CIE study determined parameters of all the phosphors under study were tabulated in Table 4.8.

Sample	Excitation Wavelength	CIE coordinates		Color Purity (%)	CCT (K)
		X	Y		
Sr_2YVO_6:1 % Eu^{3+}	278 nm	0.508	0.467	65.14	2522.41
	320 nm	0.623	0.372	83.21	1922.87
	396 nm	0.467	0.531	73.47	3363.56
	467 nm	0.411	0.543	68.01	4165.92
Sr_2YVO_6:2 % Eu^{3+}	278 nm	0.539	0.441	68.26	2089.81
	320 nm	0.628	0.366	84.24	2023.76
	396 nm	0.515	0.484	73.15	2561.62
	467 nm	0.437	0.522	66.25	3711.96
Sr_2YVO_6:3 % Eu^{3+}	278 nm	0.603	0.387	78.89	1740.47
	320 nm	0.637	0.36	86.11	2194.24
	396 nm	0.494	0.504	68.82	2897.12
	467 nm	0.456	0.504	62.27	3362
Sr_2YVO_6:4 % Eu^{3+}	278 nm	0.568	0.417	72.50	1801
	320 nm	0.638	0.358	86.54	2253.19
	396 nm	0.481	0.517	72.25	3112.5
	467 nm	0.437	0.519	62.64	3693.12
Sr_2YVO_6:5 % Eu^{3+}	278 nm	0.507	0.468	65.09	2540.43
	320 nm	0.629	0.365	84.46	2041.24
	396 nm	0.479	0.519	72.90	3152.75
	467 nm	0.438	0.521	66.16	3692.83

Table 4.8. CIE color coordinates determined parameters.

4.3.6 Thermoluminescence Studies After Beta Irradiation:

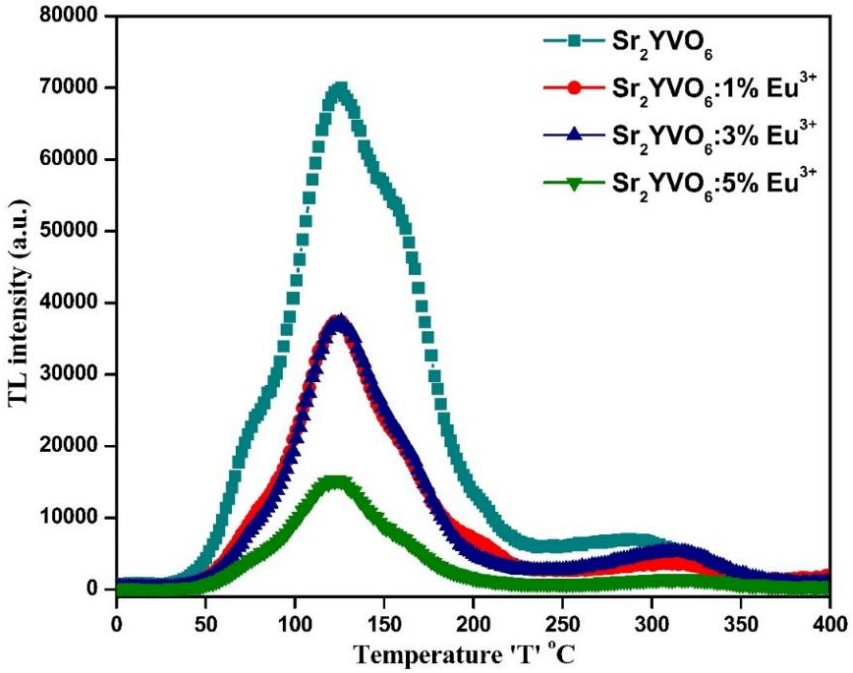

Figure 4.16. Thermoluminescence glow curves of Sr_2YVO_6:x mol% Eu^{3+} (x=0, 1, 3, 5) phosphors.

Figure 4.16 depicts the thermoluminescence glow curves of the pristine and Eu^{3+} activated Sr_2YVO_6 phosphors, in which Eu^{3+} concentrations were taken as 1 mol%, 3 mol%, and 5 mol%. In order to record the TL glow curves, all the samples were irradiated first for 10 Gy beta dose via the ^{90}Sr beta source. For each measurement, equally weighted (0.5 mg) pure and Eu^{3+} doped Sr_2YVO_6 phosphors were taken, and subsequently, the TL measurements were carried out. After the irradiation process, the glow curves are recorded within 0 °C to 400 °C by kipping constant heating of 2 °C/s. All the phosphors under investigation exhibited excellent TL behaviour at lower beta dose. From the figure, it is observed that the undoped phosphor displayed good intense TL glow curve with the highest TL intensity peak at 126 °C followed by a relatively weak glow peak at 295 °C. However, in the case of doped samples, the most intense glow peak was arisen at 124 °C, and a supplementary glow maximum towards higher temperature side with a centre temperature of 313 °C. Interestingly, when the Eu^{3+} dopant is introduced in the host material, the most intense TL peak of the host material is found to be shifted towards lower temperature, whereas, the 295 °C TL peak of the host material is shifted toward the higher temperature side.

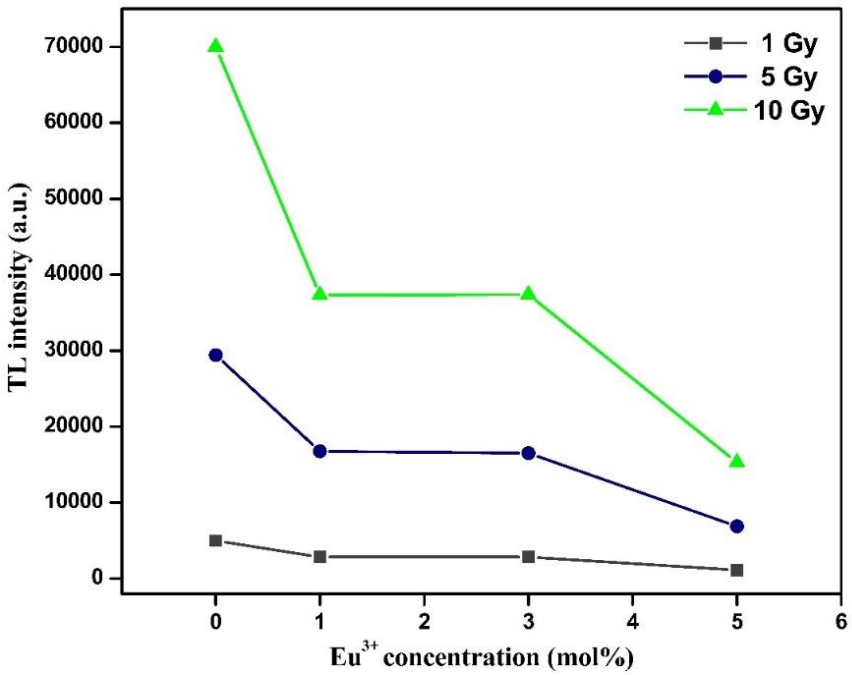

Figure 4.17. TL intensity response to different Eu^{3+} concentrations.

Among these phosphors irradiated with a 10 Gy dose of beta rays, the maximum intensity was obtained from the undoped Sr_2YVO_6 phosphor. Figure 4.17 shows the TL response to varying Eu^{3+} concentration under fixed beta doses, primarily 1, 5, and 10 Gy. Precisely, when the phosphor containing 1 mol % of Eu^{3+} undergoes TL measurements, the intensity of TL glow of the corresponding glow curves remained approximately half that of intensity counts of undoped Sr_2YVO_6. This result remained true for all the values of applied beta doses. A similar TL intensity count was observed for both 1 mol% Eu^{3+} and 3 mol% Eu^{3+} doped Sr_2YVO_6 samples. Furthermore, as the Eu^{3+} doping level is increased by 5 mol%, a further decrement in TL intensity is observed. Consequently, a higher concentration of Eu^{3+} impurities within the host matrix Sr_2YVO_6 leads to increasing TL intensity quenching, possibly due to the seven unpaired electrons of Eu^{3+} [43,44]. The cause of intensity quenching due to the increasing doping level following perturbation in the dopant's energy levels, which was then resulted in TL intensity quenching [45].

The linear dose response of phosphor samples with steadily increasing doses of ionizing radiation is a crucial parameter for a material to be employed as a TL dosimeter. Ideally, in an acceptable TLD material, the absorbed dose of ionizing radiation should exhibit a direct proportionality to the TL response [46]. With these facts keeping in mind, the prepared series of double perovskite phosphors were exposed to various doses of beta ionizing radiation, specifically 1, 5, and 10 Gy. The TL glow curves for both pure and Eu^{3+} activated Sr_2YVO_6

phosphors under the mentioned doses of beta rays were recorded using a steady heating of 2 °C/s, presented in Figure 4.18.

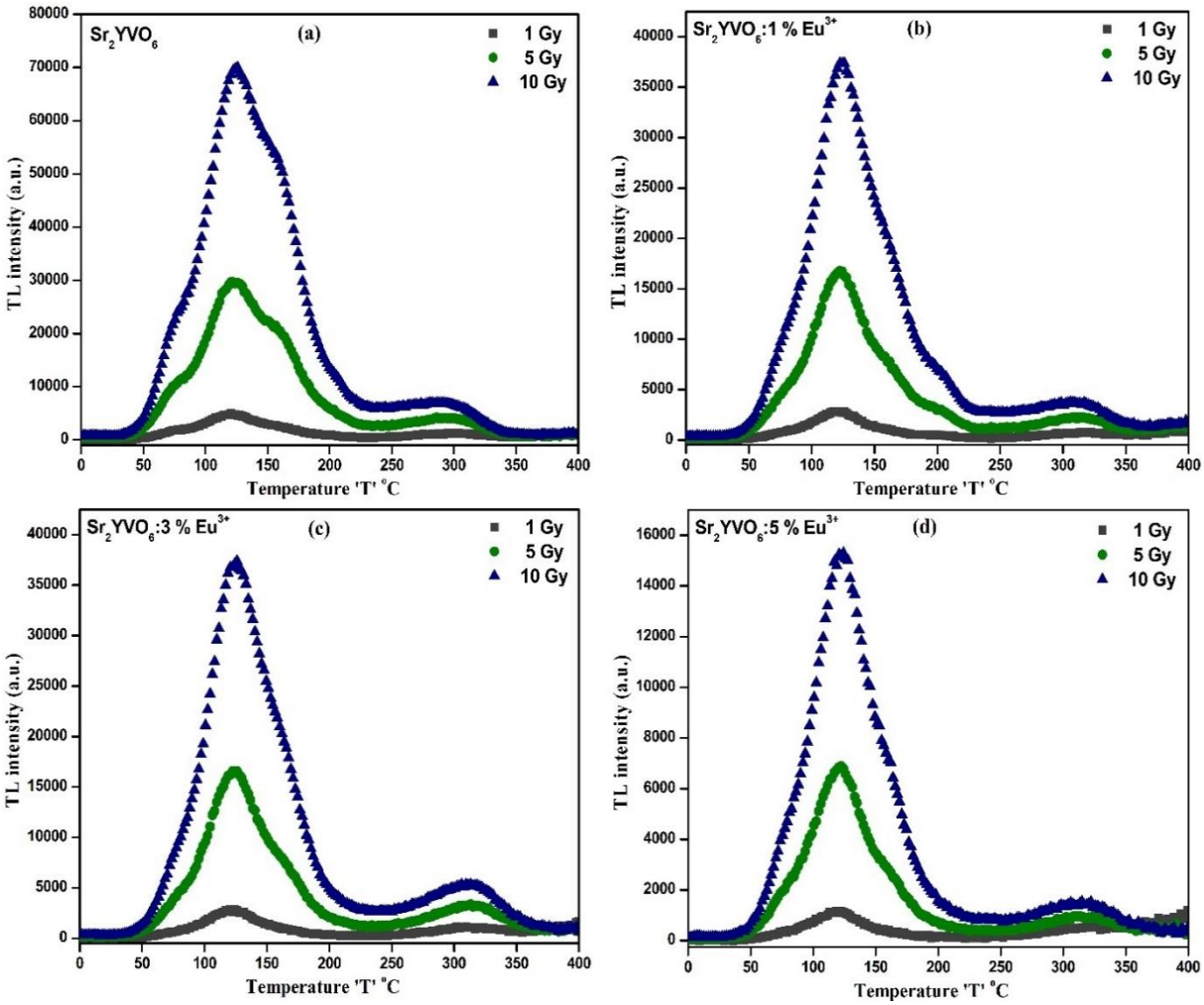

Figure 4.18. TL glow curves of Sr_2YVO_6:x mol% Eu^{3+} (x=0, 1, 3, 5) phosphors at different beta doses.

Upon different times of radiation exposures corresponding to different doses, the glow peak location and glow curve nature exhibited prominent similarities. However, a gradual enhancement in TL intensity was observed with rising dose of beta rays. This growth in the TL glow intensity with increasing dose of beta rays signifies the progressive generation of vacancies. This phenomenon can be associated with the increasing rate of recombination of trapping centres, consequently leading to a rise in the TL glow intensity [47,48].

The linear dose response within the 1 to 10 Gy range of beta ray exposure can be explained by examining an intensity versus beta dose plot, as illustrated in Figure 4.19. This observed linear relationship between TL intensity and the increment in beta dose suggests a progressive increase in defect formation in response to beta ionizing radiation. This increase in TL glow is related to an increase in the population of trapping centres [49].

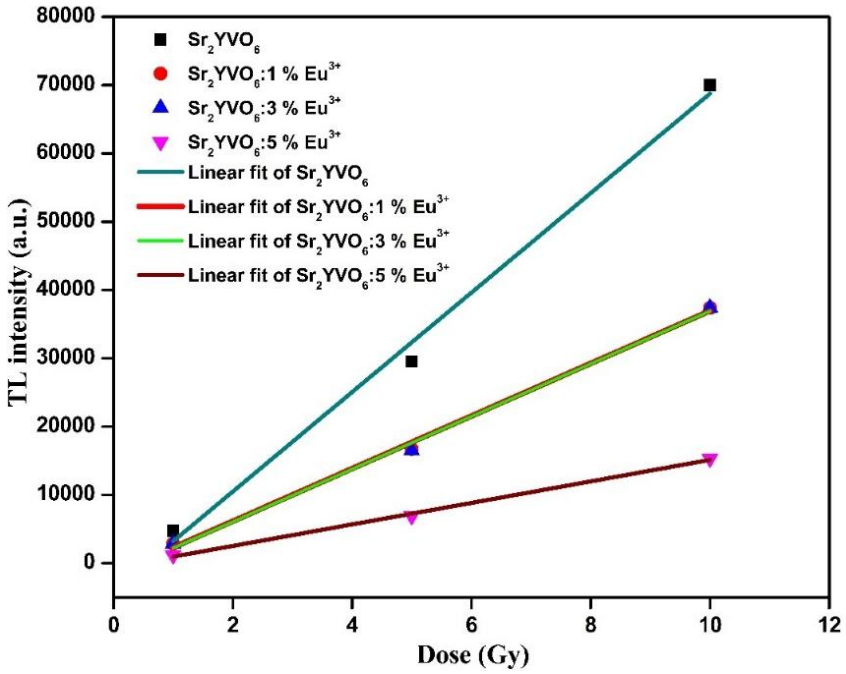

Figure 4.19. TL response of undoped and Eu^{3+} doped Sr_2YVO_6 phosphors to beta irradiation.

To investigate the kinetic features of the phosphor material, it is essential to analyze the acquired TL glow curve. By examining the experimental TL glow curves, valuable information about trap centres and trapping parameters can be obtained. In TL studies, the determination of trapping parameters, which include activation energy, frequency factor, and the order of kinetics, is crucial for understanding the TL properties of the prepared luminescent material. Numerous methods have been developed for evaluating the kinetic parameters of TL glow curves. In this study, the kinetic features of the sample materials were ascertained by calculating the kinetic parameters using two methods: Chen's peak shape method (PSM) and computerized glow curve deconvolution (CGCD) method.

Initially, the acquired glow curves of both undoped and Eu^{3+} doped Sr_2YVO_6 samples, which were exposed to a 10 Gy dose of beta rays, were subjected to analysis using Chen's PSM. In order to apply PSM, first the TL glow curves needed to be deconvoluted. This analysis allowed the calculation of kinetic parameters for all the deconvoluted peaks present within a single glow curve of each doped and undoped sample. It is important to note that this method does not require information on the order of kinetics. This method is essentially based on three equations of temperature parameters, which are τ (low-temperature half-width), δ (high-temperature half-width), and ω (Full-width at half maximum intensity), and were applicable for any order of kinetic [50,51].

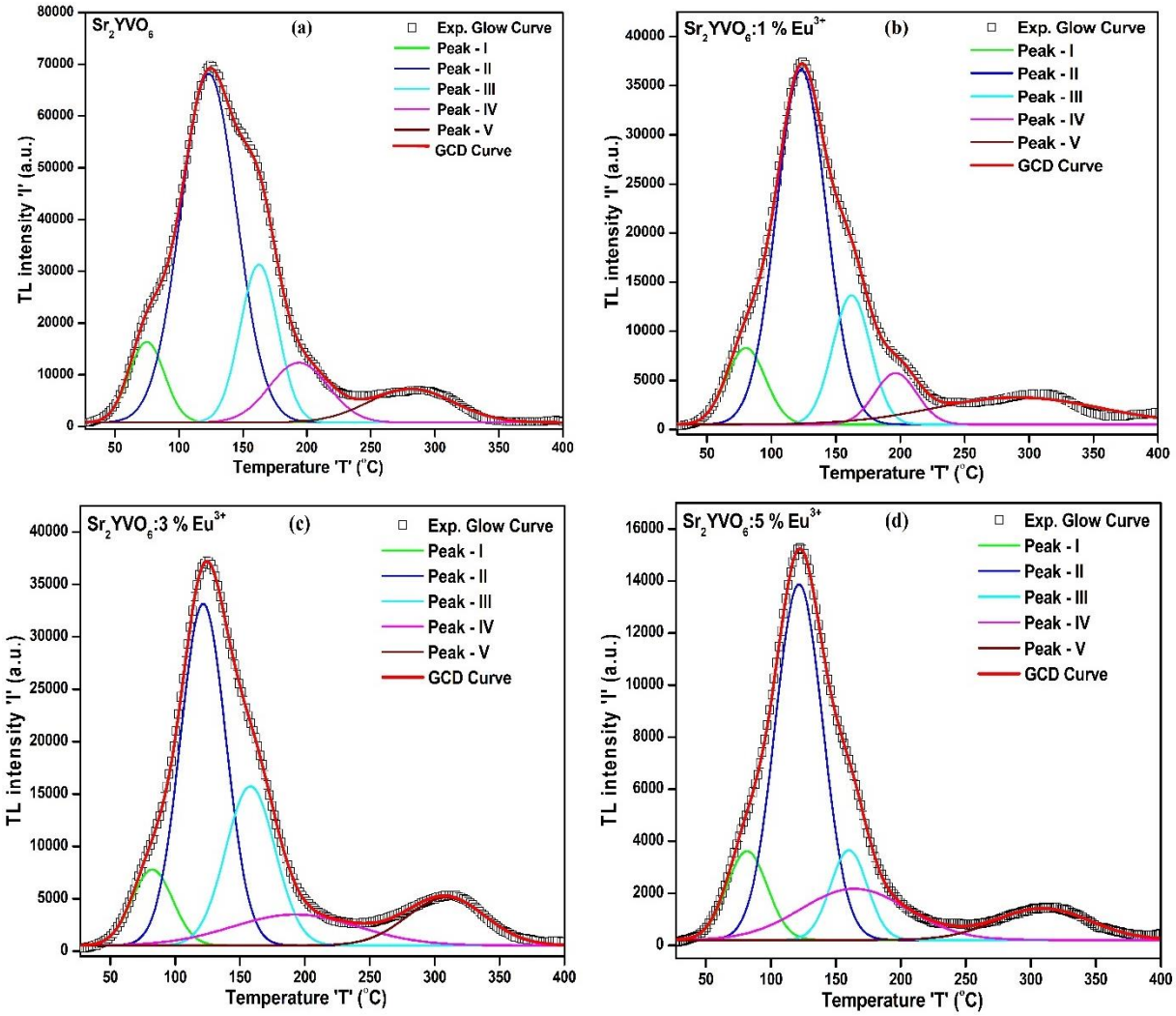

Figure 4.20. Deconvoluted TL glow curves of Sr_2YVO_6:x mol% Eu^{3+} (x=0, 1, 3, 5) phosphors after beta irradiation of 10 Gy.

The experimental TL glow curves of the samples were subjected to fitting using the Glow Curve Deconvolution (GCD) method, revealed the presence of five distinct glow peaks with peak temperatures of 75 °C, 124 °C, 162 °C, 193 °C, and 280 °C, as depicted in Figure 4.20. The values for the geometrical factor all five deconvoluted peaks identified, were found to be in the range of 0.47 to 0.51, which closely aligns with the value proposed by Chen for general-order kinetics [52]. Consequently, the determination of trap depths for all five of these deconvoluted peaks was accomplished using Chen's activation energy equation for the glow curve following general-order kinetics. The calculated values for activation energy E_τ, E_δ, and E_ω of all the peaks identified in deconvoluted curves fall within the ranges of 0.36-1.47 eV, 0.49-1.63 eV, and 0.43-1.55 eV, respectively. A complete tabulation of all the determined parameters using the PSM is tabulated in Table 4.9.

Additionally, the Computerized Glow Curve Deconvolution (CGCD) method was employed for the trapping parameter calculation, wherein the same deconvoluted curves were taken into account. In order to discover the kinetic features of the glow curves and determine their order of kinetics, several equations were developed by Kitis et al., for any available order of kinetics [53]. Consequently, it was predictable that the order of kinetics for the prepared samples under study is general order kinetics. By utilizing the Kitis et al. formula of general order kinetics (equation 3.15), the activation energy of all five deconvoluted peaks was calculated. Moreover, another trap parameter namely frequency factor (s), can also be computed by applying frequency factor formula applicable to general order kinetic (equation 3.18).

The determined activation energy for samples irradiated with a 10 Gy dose, including the host Sr_2YVO_6 and Sr_2YVO_6:x mol% Eu^{3+} (where x= 1, 3, 5) samples, falls within the range of 0.36±0.02 eV to 1.48±0.07 eV. A complete demonstration of all the TL kinetics parameters obtained through CGCD was tabulated in Table 4.10. The trap parameters calculated using both the PSM and the GCD method were comparable.

Sample		I_{max}	T_{max} (K)	T_1 (K)	T_2 (K)	τ (K)	δ (K)	ω (K)	μ_g	Activation Energy		
										E_τ (eV)	E_δ (eV)	E_ω (eV)
Sr_2YVO_6	Peak I	16320	348.6	331.1	364.6	17.5	16	33.5	0.48	0.96±0.06	1.11±0.07	1.05±0.03
	Peak II	68122	397.2	369.5	422	27.7	24.8	52.5	0.47	0.75±0.03	0.93±0.04	0.84±0.02
	Peak III	31288	435.8	417.3	453	18.59	17.11	35.7	0.48	1.44±0.08	1.63±0.1	1.55±0.05
	Peak IV	12351	466.8	438	495.3	28.84	28.46	57.3	0.50	1.01±0.03	1.13±0.04	1.08±0.02
	Peak V	7266	553	512.4	597.2	40.6	44.2	84.8	0.52	0.98±0.02	1.02±0.02	1.00±0.01
Sr_2YVO_6: 1 mol% Eu^{3+}	Peak I	8307	354	334.2	372	19.8	18	37.8	0.48	0.87±0.04	1.03±0.06	0.95±0.03
	Peak II	36612	395.4	372.5	418	22.9	22.6	45.5	0.50	0.92±0.04	1.02±0.05	0.98±0.02
	Peak III	13631	434.9	416.7	453.3	18.2	18.4	36.6	0.50	1.47±0.08	1.51±0.08	1.50±0.04
	Peak IV	5753	469	447.1	491.3	21.9	22.3	44.2	0.50	1.40±0.07	1.45±0.07	1.44±0.03
	Peak V	3271	564.6	476.2	647.3	88.4	82.7	171.1	0.48	0.36±0.01	0.57±0.01	0.47±0.01
Sr_2YVO_6: 3 mol% Eu^{3+}	Peak I	7789	362.8	335.3	373.7	20.5	17.9	38.4	0.47	0.84±0.04	1.04±0.06	0.94±0.02
	Peak II	33148	395.4	373.4	414.6	21.93	19.2	41.13	0.47	0.98±0.04	1.20±0.06	1.09±0.03
	Peak III	15732	431.4	407	453.5	24.4	22.1	46.5	0.48	1.04±0.04	1.24±0.06	1.15±0.02
	Peak IV	3489	465.6	400.8	530.4	64.8	64.8	129.6	0.50	0.36±0.01	0.49±0.01	0.43±0.01
	Peak V	5112	582.6	543	620.4	39.6	37.8	77.4	0.49	1.13±0.03	1.32±0.03	1.24±0.02
Sr_2YVO_6: 5 mol% Eu^{3+}	Peak I	3617	355.8	336	373.3	19.8	17.5	37.3	0.47	0.87±0.05	1.07±0.06	0.97±0.03
	Peak II	13866	395.4	373.2	415.8	22.2	20.4	42.6	0.48	0.96±0.04	1.13±0.06	1.05±0.03
	Peak III	3657	433.2	414.5	450.5	18.7	17.3	36	0.48	1.41±0.08	1.60±0.09	1.52±0.05
	Peak IV	2176	438	384	489	54	51	105	0.49	0.40±0.01	0.55±0.01	0.48±0.01
	Peak V	1419	582.6	534	631.7	48.6	49.1	97.7	0.50	0.89±0.02	1.02±0.02	0.96±0.01

Table 4.9. Summary of TL kinetic parameters calculated by PSM.

Sample		T_{max} (K)	Activation Energy 'E_a' (eV)	Order of Kinetics 'b'	FOM %	Frequency Factor 's' (s^{-1})
Sr_2YVO_6	Peak I	348.6	0.95±0.02	2.0	3.34	9.82×10^{11}
	Peak II	397.2	0.75±0.06	1.70		3.33×10^{7}
	Peak III	435.8	1.41±0.02	1.65		3.62×10^{14}
	Peak IV	466.8	1.01±0.02	2.0		8.89×10^{8}
	Peak V	553	0.97±0.02	1.25		3.37×10^{6}
Sr_2YVO_6: 1 mol% Eu^{3+}	Peak I	354	0.85±0.03	2.0	3.74	1.85×10^{10}
	Peak II	395.4	0.92±0.06	1.70		6.62×10^{9}
	Peak III	434.9	1.48±0.02	1.65		2.98×10^{15}
	Peak IV	469	1.39±0.02	1.70		1.42×10^{9}
	Peak V	564.6	0.36±0.02	0.90		4.44×10^{7}
Sr_2YVO_6: 3 mol% Eu^{3+}	Peak I	362.8	0.72±0.03	2.0	2.82	1.24×10^{8}
	Peak II	395.4	0.98±0.05	1.70		4.10×10^{10}
	Peak III	431.4	1.01±0.02	1.65		7.78×10^{12}
	Peak IV	465.6	0.35±0.02	1.60		2.02×10^{7}
	Peak V	582.6	1.15±0.02	1.49		6.04×10^{7}
Sr_2YVO_6: 5 mol% Eu^{3+}	Peak I	355.8	0.91±0.03	2.0	2.94	1.30×10^{11}
	Peak II	395.4	0.95±0.07	1.70		1.77×10^{10}
	Peak III	433.2	1.35±0.01	1.65		8.34×10^{13}
	Peak IV	438	0.43±0.01	1.60		4.17×10^{7}
	Peak V	582.6	0.87±0.01	1.49		1.80×10^{5}

Table 4.10. Summary of TL kinetic parameters calculated by GCD method.

4.3.7 Thermoluminescence Studies After UV Irradiation:

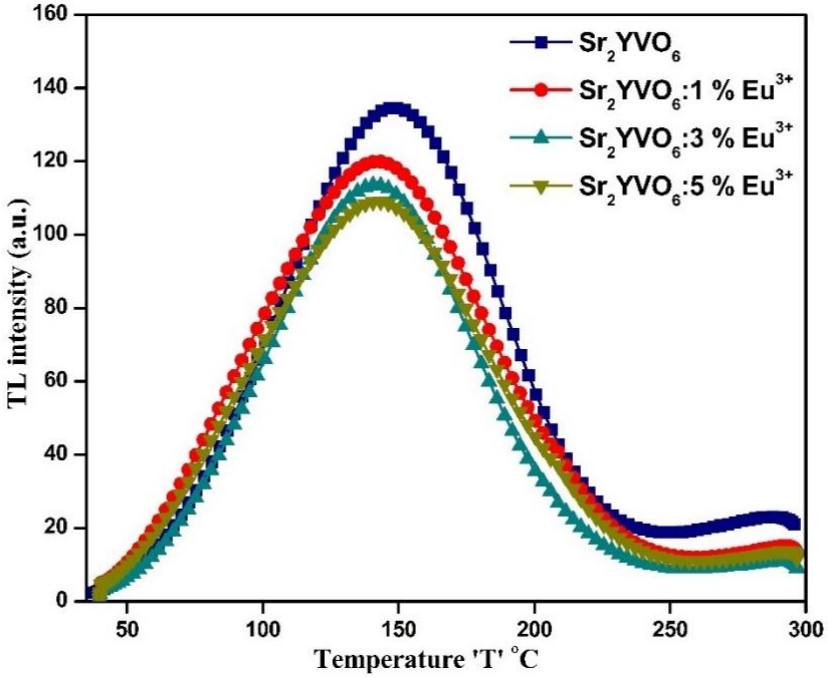

Figure 4.21. TL glow curves of $Sr_2YVO_6:Eu^{3+}$ phosphors along with undoped Sr_2YVO_6 when exposed to UV irradiation for 60 min.

Figure 4.21 illustrates the acquired TL glow curves of undoped and Eu^{3+} doped Sr_2YVO_6 double perovskites when irradiated for 60 min with UV radiation. Equally weighted (0.5 mg) undoped and Eu^{3+} doped Sr_2YVO_6 phosphors were taken for the TL measurements. The TL measurements of the all the phosphors under study were taken after six different times of UV exposures, primarily, 10 min, 20 min, 30 min, 40 min, 50 min, and 60 min. First, in order to examine the TL behaviour from the phosphors under study, the TL glow curves were recorded with a steady heating rate of 2 °C/s from room-temperature to 300 °C after 60 min of UV exposure period. In the case of undoped phosphor, within of 35 °C to 250 °C temperature region, a very nice bell-shaped TL glow curve with a centre temperature of roughly 150 °C was observed. Whereas, in the case of doped samples, a similar single peaked TL glow curve with centre temperature around 140 °C is observed. As the dopant concentration increases, TL intensity marginally decreases, and the peak temperature shifts from 150 °C to 140 °C. This may be due to the increase in Eu^{3+} concentration, wherein Y^{3+} is replaced by Eu^{3+} leads to imbalance in site symmetry. In addition, the intensity reduction can also be taking place because of the seven unpaired electrons of Eu^{3+} [13,45]. In this study, the maximum TL intensity is observed for undoped Sr_2YVO_6 phosphor. Similar to the TL study carried out after beta irradiation, we observed good TL response after UV irradiation from the undoped sample among all studied. This is such that the TL characteristics of the phosphor can be affected by

ionizing radiation in addition to activators. The most crucial factor in TL characterization is any ionizing radiation exposure [54,55].

Under any given time of UV exposure period among the six mentioned (10-60 min), undoped Sr_2YVO_6 phosphor exhibited maximum intensity. The intensity of the TL glow curve decreased when 1 mol% of Eu^{3+} was doped into the host lattice Sr_2YVO_6. The TL intensity further decreased when the phosphor was doped by 3 mol% of Eu^{3+}. This is because the introduction of Eu^{3+} destroys the previously created traps due to its unpaired electrons, which was then apparent in the reduction in TL intensity. Moreover, 5 mol% doping of Eu^{3+} further reduces the TL glow due to the concentration quenching. The phenomenon of concentration quenching is seen as the dopant concentration rises above the threshold value. In the present phosphor system, 1 mol% doping of Eu^{3+} serves as the threshold. At higher Eu^{3+} concentrations, the distance between successive dopant ions decreases due to the excess number of dopant ions, which then perturbs the dopant's energy levels and causes intensity quenching [45].

The exposure to UV radiation creates the surface defects other than the deeper traps produced by the high-energy ionizing radiation, such as alpha, beta and gamma rays. In order to understand the effect of the UV exposure on the rigid perovskite structure, the samples were irradiated for different times of UV exposure, primarily 10 to 60 min, in intervals of 10 minute, as shown in Figure 4.22.

From the figure, it is observed that the intensity of TL rises with increasing UV exposure time. The same is true for the host as well as increasing Eu^{3+} concentration. For all the phosphors under investigation, the maximum intensity is observed after being subjected to UV irradiation for forty min. Later, the TL intensity gets quenched by ~20% for a longer exposure time than the one mentioned. In the present phosphor system, fifty minute of UV irradiation resulted in a fall in TL intensity. The overpopulation of traps (electron-hole pairs) created due to heavy UV irradiation leads to non-radiative de-trapping, resulting in suppuration in TL glow, which is observed for 50 min and 60 min time of UV irradiation [56,57].

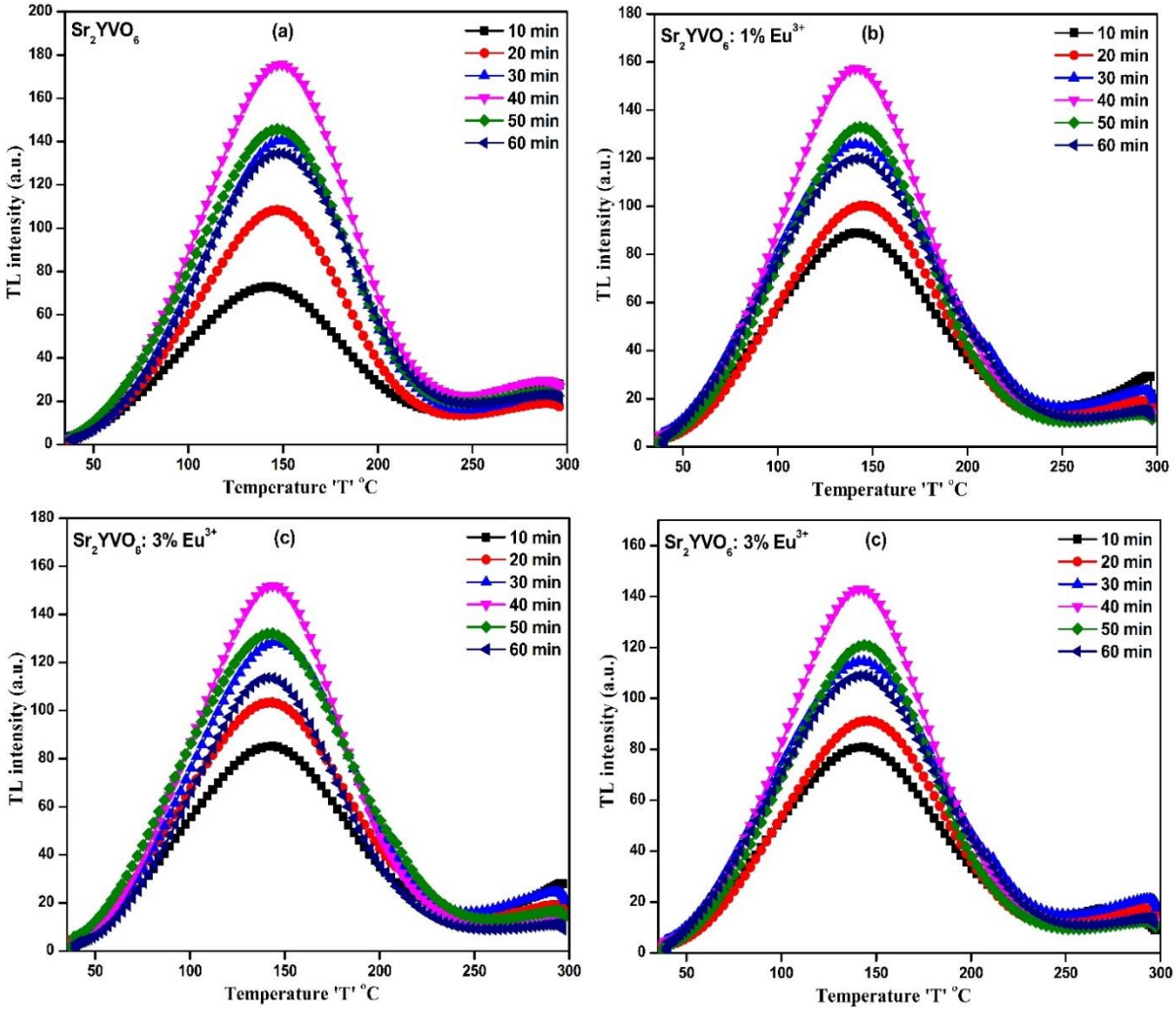

Figure 4.22. TL glow curves of Sr_2YVO_6:Eu^{3+} phosphors at different at different UV exposure time.

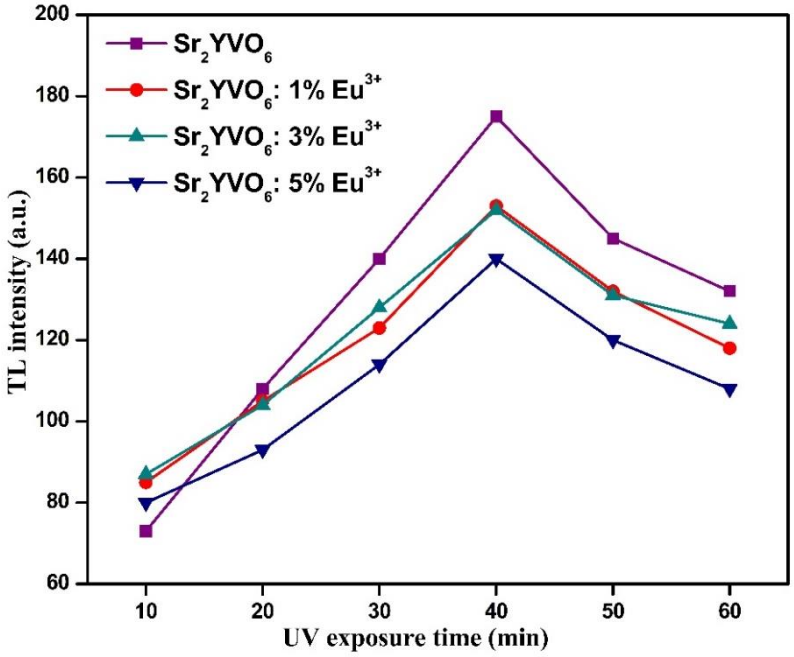

Figure 4.23. Plot of TL intensity vs. UV exposure period.

In order to understand the dosimetry feature towards lower energy radiation (UV-rays) of the phosphor under investigation, the linear response of the TL intensity with a rising exposure period is the necessary condition. To check the TL response from the Sr_2YVO_6 phosphors, whether is linear or not, the plot of TL intensity as a function of the UV exposure period was drawn, and the results are depicted in Figure 4.23. Dose-response looks linear up to 40 mins UV exposure time for all undoped and doped Sr_2YVO_6 phosphors. The obtained results from the dose response indicate that the phosphor is may beneficial for dosimetry applications towards UV rays, because it has a linear dose response up to a particular time of UV exposure [58,59].

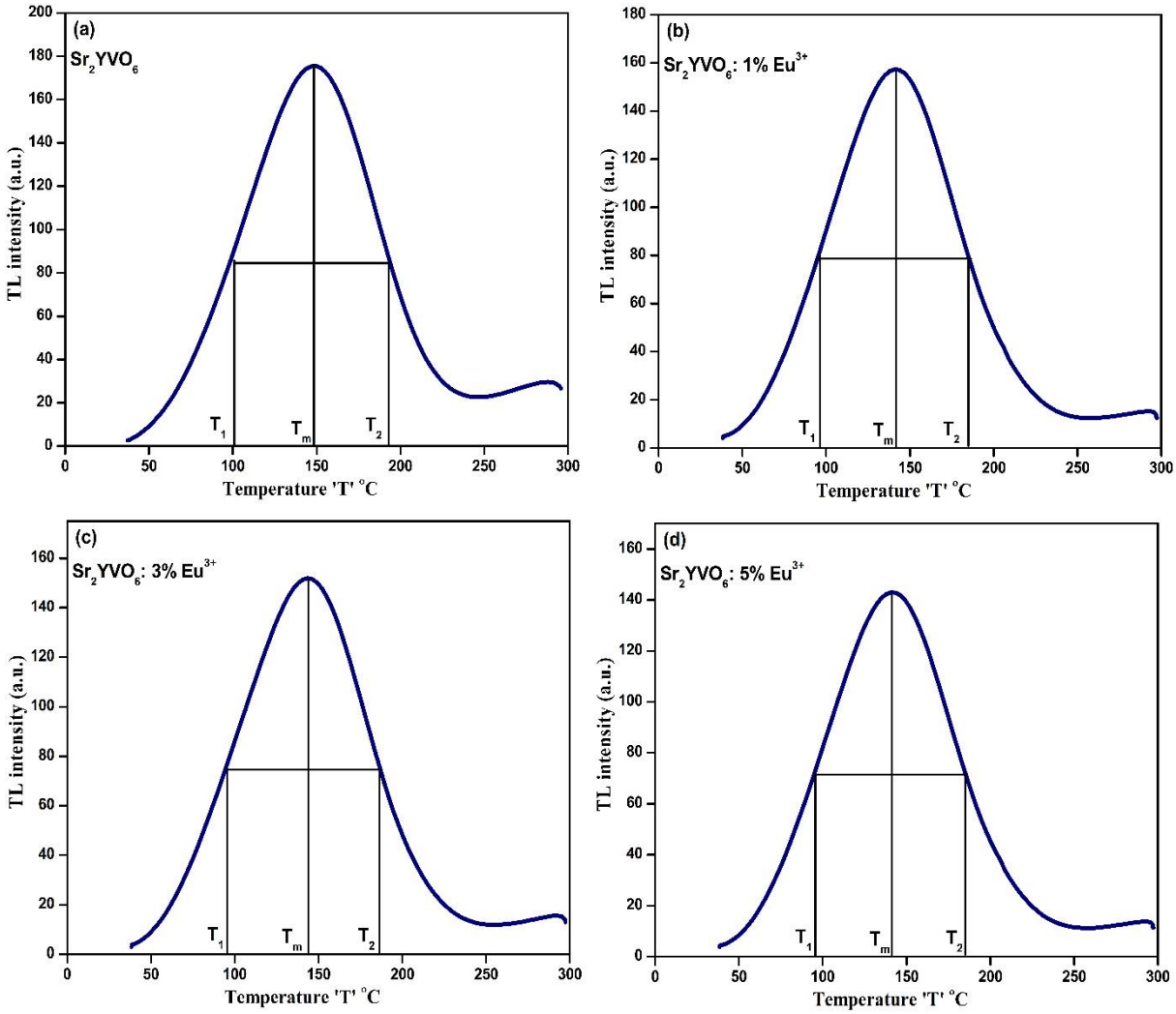

Figure 4.24. TL glow curves of Undoped and Eu^{3+}doped Sr_2YVO_6 phosphors with PSM notations.

Analysis of the experimental TL glow curves was done for information about the trapping centres and trapping parameters associated with it. In the present case, with the glow

curve having a single glow peak, we considered Chen's peak shape method (PSM) for trapping parameter determination. Figure 4.24 depicts the glow curves of the Sr_2YVO_6 phosphors with the notations of the peak shape method notations. The geometrical factor suggests that the kinetic order of all $Sr_2YVO_6:Eu^{3+}$ glow curves is second-order kinetics [60,61]. By means of the general equation of trapping parameter determination suggested by Chen, the activation energies were calculated. Table 4.11 displays the estimated kinetic parameters from the peak shape approach.

Sample	T_{max} (K)	T_1 (K)	T_2 (K)	τ (K)	δ (K)	ω (K)	μ_g	Activation Energy		
								E_τ (eV)	E_δ (eV)	E_ω (eV)
Pure	420	373	469	48	48	96	0.50	0.42±0.01	0.54±0.01	0.48±0.01
1 % Eu^{3+}	414	368	460	46	46	92	0.50	0.43±0.01	0.54±0.01	0.49±0.01
3 % Eu^{3+}	415	368	462	47	47	94	0.50	0.43±0.01	0.54±0.01	0.49±0.01
5 % Eu^{3+}	414	368	461	46	47	93	0.51	0.44±0.01	0.54±0.01	0.49±0.01

Table 4.11. Summary of TL kinetic parameters of Sr_2YVO_6 phosphors irradiated by UV-radiation for 40 min calculated by PSM.

References:

1. L. Perez-Cruz, E. Cruz-Zaragoza, D. Diaz et al., Synthesis, optical and thermoluminescence properties of thulium-doped $KMgF_3$ fluoroperovskite, *Appl. Radia. Isotop.* **177** (2021) 109913.
2. N. Mandlik, P. Sahare, M. Kulkarni, Study of optically stimulated luminescence and calculation of trapping parameters of $K_2Ca_2(SO_4)_3$:Eu nanophosphor, *Appl. Radia. Isotop.* **167** (2021) 109388.
3. M. Sen, R. Shukla, V. Sathian et al., Thermoluminescence based personnel neutron dosimetry study of $LiMgBO_3:Dy^{3+}$, *Cera. Inter.* **46** (2020) 20236-20242.
4. A. Kumar, A. Kumar, R. Dogra et al., Investigation of thermoluminescence and kinetic parameters of gamma ray exposed LiF: Sm^{3+}, Eu^{3+} nanophosphors for dosimetric applications, *Cera. Inter.* **44** (2018) 15535-15541.
5. A. Ozdemir, V. Guckan, V. Altunal et al., Thermoluminescence in MgB4O7:Pr,Dy dosimetry powder synthesized by solution combustion synthesis method, *J. Lumin.* **230** (2021) 117761.
6. M. Bakr, Z. Portakal, M. Yuksel et al., Thermoluminescence properties of beta particle irradiated $Ca_3Al_2O_6$ phosphor relative to environmental dosimetry, *J. Lumin.* **227** (2020) 117565.
7. Z. Portakal-Ucar, U. kaynar, T. Dogan et al., Thermoluminescence behaviour of europium doped magnesium silicate after beta exposure, *Opt. Mater.* **104** (2020) 109852.
8. H. Lokesha and M. Chithambo, A combined study of the thermoluminescence and electron paramagnetic resonance of point defects in $ZrO_2:Er^{3+}$, *Radia. Phys. Chem.* **172** (2020) 108767.
9. R. Tamrakar, K. Upadhyay and M. Sahu, Model to explain the concentration quenching on thermoluminescence behaviour of Eu^{3+} doped Gd_2O_3 phosphor under UV irradiation, *J. Alloy. Comp.* **699** (2017) 898-906.
10. R. Tamarakar, D. Bisen, K. Upadhyay et al. Synthesis and thermoluminescence behavior of $ZrO_2:Eu^{3+}$ with variable concentration of Eu^{3+} doped phosphor, *J. Radia. Res. Appl. Sci.* **7** (2014) 486-490.
11. A. Verma and A. Verma, Synthesis, characterization, mechano-luminescence, thermoluminescence, and antibacterial properties of $SrMgAl_{10}O_{17}$:Eu phosphor, *J. Alloy. Comp.* **802** (2019) 394-408.

12. N. Dubey, V. Dubey, J. Saji et al., Thermoluminescence glow curve analysis and trap parameters calculation of UV-induced $La_2Zr_2O_7$ phosphor doped with gadolinium, *J. Mater. Sci: Mater. Electron.* **31** (2020) 1936-1944.
13. N. Degda, N. Patel, V. Verma et al., Photoluminescence and thermoluminescence kinetic features of Eu^{3+} doped Sr_2YVO_6 double perovskite phosphor, *Opt. Mater.* **142** (2023) 114019.
14. Y. Alsabah, A. Elden, M. Alsalhi et al., Structural and optical properties of A_2YVO_6 (A = Mg, Sr) double perovskite oxides, *Results Phys.* **15** (2019) 102589.
15. S. Chaki, M. Chaudhary, and M. Deshpande, Effect of indium and antimony doping in SnS single crystals, *Mater. Res. Bull.* **63** (2015) 173-180.
16. C. Wei, D. Xu, J. Li et al., Synthesis and luminescence properties of Eu^{3+}-doped a novel double perovskite Sr_2YTaO_6 phosphor, *J. Mater. Sci: Mater. Electron.* **30** (2019) 2864-2871.
17. M. Kusuma and G. Chadrappa, Effect of calcination temperature on characteristic properties of $CaMoO_4$ nanoparticles, *J. Sci: Adv. Mater. Devic.* **4** (2019) 150-157.
18. G. Apsana, P. P. George, N. Devanna et al., BIOMIMETIC SYNTHESIS AND ANTIBACTERIAL PROPERTIES OF STRONTIUM OXIDE NANOPARTICLES USING OCIMUM SANCTUM LEAF EXTRACT, *Asian J. Pharma. Clinic. Res.* **11** (2018) 384.
19. B. N. Lakshminarasappa, N. J. Shivaramu, K. R. Nagabhushana et al., Synthesis characterization and luminescence studies of 100 MeV Si^{8+} ion irradiated sol gel derived nanocrystalline Y_2O_3, *Nucle. Instru. Metho. Physi. Res. B.* **329** (2014) 40-47.
20. O. Meza, E. Villabona-Leal, L. Diaz-Torres et al., Luminescence Concentration Quenching Mechanism in Gd_2O_3:Eu^{3+}, *J. Phys. Chem. A* **118** (2014) 1390-1396.
21. J. Dai, M. Lv, G. Li et al., Synthesis and luminescence properties of highly uniform SiO2@$LaPO_4$:Eu^{3+} core-shell phosphors, *Mater. & Design* **83** (2015) 795-800.
22. D. Sevic, M. Rabasovic, J. Krizan et al., Characterization and luminescence kinetics of Eu^{3+} doped YVO_4 nanopowders, *Mater. Res. Bull.* **88** (2017) 121-126.
23. T. Zhao, N. Chen, G. Du et al., Effect of Ba^{2+} doping on the photoluminescence of YVO_4:Eu^{3+} phosphor and first principles calculations, *J. Lumin.* **222** (2020) 117117.
24. A. Setlur, H. Comanzo, A. Srivastava et al., Spectroscopic Evaluation of a White Light Phosphor for UV-LEDs-$Ca_2NaMg_2V_3O_{12}$:Eu^{3+}, *J. Electrochem. Soc.* **152** (2005) H205.

25. Q. Chen, B. Miao, P. Suthanthira Kumar et al., Enhanced luminescence properties and Judd-Ofelt analysis of novel red emitting $Sr_2LiScB_4O_{10}:Eu^{3+}$ phosphors for WLED applications, *Opt. Mater.* **116** (2021) 111093.
26. N. Safronova. R. Yavestskiy, O. Kryzhanovska et al., Fabrication and VUV luminescence of $Lu_2O_3:Eu^{3+}$ (5 at.%) nanopowders and transparent ceramics, *Opt. Mater.* **101** (2020) 109730.
27. H. Tseng, W. Tzou, S. Wei et al., Effects of synthesis temperature and Eu_2O_3 concentration on the crystalline phases and photoluminescence properties of $SrAl_2O_4$ phosphors, *J. Mater. Res. Technol.* **9** (2020) 14051-14060.
28. R. Krishnan, R. Kroon, and H. Swart, Charge transfer characteristics and luminescence properties of Eu^{3+} activated Ba_2YMoO_6 and $BaY_2(MoO_4)_4$ phosphors, *Mater. Res. Bull.* **145** (2022) 111554.
29. X. Wu, W. Bai, O. Hai et al., Crystal structure and luminescence properties of a novel red $Ca_3GdNa(PO_4)_3F:Eu^{3+}$ phosphor for white LEDs, *Optic. Laser technol.* **107** (2018) 46-53.
30. B. Fan, J. Liu, W. Zhou et al., Luminescence properties of new red-emitting phosphor $Li_2Al_2Si_3O_{10}:Eu^{3+}$ for near UV-based white LED, *Opt. Mater.* **98** (2019) 109499.
31. A. Vishwakarma, K. Jha, M. Jayasimhadri et al., Red light emitting $BaNb_2O_6:Eu^{3+}$ phosphor for solid state lighting applications, *J. Alloy. Comp.* **622** (2015) 97-101.
32. S. Wang, M. Chen, S. Lan et al., Finding a novel $Ca_2M_3(SiO_4)_2(PO_4)O$ (M = La, Y):Eu^{3+} red-emitting phosphor with positive responsiveness to phytochrome: Application in plant cultivation, *J. Lumin.* **237** (2021) 118151.
33. T. Wang, X. Xu, D. Zhou et al., Red phosphor $Ca_2Ge_7O_{16}:Eu^{3+}$ for potential application in field emission displays and white light-emitting diodes, *Mater. Res. Bull.* **60** (2014) 876-881.
34. Y. Tian, Development of phosphors with high thermal stability and efficiency for phosphor-converted LEDs, *J. Sol. State Light* **1** (2014) 11.
35. G. Annadurai, B. Devakumar, H. Guo et al., Photoluminescence properties of novel $Ba_2Lu_5B_5O_{17}:Eu^{3+}$ red emitting phosphors with high color purity for near-UV excited white light emitting diodes, *RSC Adv.* **8** (2018) 30396-30403.
36. Q. Tang, T. Yang, B. Guo et al., Synthesis and photoluminescence properties of Eu^{3+} doped $Sr_5Nb_4O_{15}$ red-emitting phosphors for white LEDs, *Optik* **224** (2020) 165770.

37. D. Golja and F. Dejene, Effect of Eu^{3+} ion concentration on the structural and photoluminescence properties of $Ba_{1.3}Ca_{0.7}SiO_4$ ceramic-based red phosphors for solid-state lighting applications, *J. Alloy. Comp.* **827** (2020) 154216.
38. D. Navami, R. Basavaraj, S. Sharma et al., Rapid identification of latent fingerprints, security ink and WLED applications of $CaZrO_3:Eu^{3+}$ fluorescent labelling agent fabricated via bio-template assisted combustion route, *J. Alloy. Comp.* **762** (2018) 763-779.
39. J. Sun and D. Cui, Synthesis, Structure, and Thermally Stable Luminescence of Dy^{3+}-Doped $Na_3YSi_2O_7$ Host Compound, *J. Americ. Ceram. Soc.* **97** (2013) 843-847.
40. G. Rajkumar, V. Ponnusamy, G. Kanmani et al., A new perovskite type Ba_2YZrO_6: Eu^{3+} red phosphor with cubical morphology for WLEDs applications, *J. Lumin.* **227** (2020) 117561.
41. N. Bhagya, P. Prashanth, R. Hari Krishna et al., Photoluminescence studies of Eu^{3+} activated $SrTiO_3$ nanophosphor prepared by solution combustion approach, *Optik* **145** (2017) 678-687.
42. V. Dubey, J. Kaur, S. Agrawal et al., Effect of Eu^{3+} concentration on photoluminescence and thermoluminescence behavior of $YBO_3:Eu^{3+}$ phosphor, *Superlattices Microstruc.* **67** (2014) 156-171.
43. G. Nair, S. Tamboli, S. Dhoble et al., Comparison of the thermoluminescence properties of $NaCaPO_4:Dy^{3+}$ phosphors irradiated by 75 MeV C^{6+} ion and γ-rays, *J. Lumin.* **224** (2020) 117274.
44. N. Mandlik, P. Sahare, S. Rondiya et al., Characteristics of $K_2Ca_2(SO4)_3$:Eu TLD nanophosphor for its applications in electron and gamma rays dosimetry, *Opt. Mater.* **109** (2020) 110272.
45. N. Degda, N. Patel, V. Verma, M. Srinivas, K.V.R. Murthy, D. Haranath, Europium doped Sr_2YNbO_6 double perovskite phosphor for photoluminescence and thermoluminescence properties, *Luminescence* **38** (2023) 176-187.
46. D. Joseph Daniel, U. Madhusoodanan, O. Annalakshmi et al., Thermoluminescence dosimetric characteristics on cubic fluoroperovskite single crystal ($KMgF_3:Eu^{2+}$, Ce^{3+}), *Opt. Mater.* **45** (2015) 224-228.
47. O. Annalakshmi, M. Jose, U. Madhusoodanan et al., Thermoluminescence dosimetric characteristics of thulium doped ZnB_2O_4 phosphor, *J. Lumin.* **146** (2014) 295-301.

48. S. Jakathamani, O. Annalakshmi, M. Jose et al., Thermoluminescence dosimetric characteristics of terbium doped barium metaborate phosphors, *Radia. Phys. Chem.* **187** (2021) 109544.
49. J. Benavente, J. Gomez-Ros and V. Correcher, A kinetic model for the thermoluminescent high dose response of LiF:Mg, Cu,P (MCP-N), *Appl. Radia. Isotop.* **170** (2021) 109634.
50. A. Kadam, G. Mishra and S. Dhoble, Thermoluminescence study and evaluation of trapping parameters $CaTiO_3$: RE (RE=Eu^{3+}, Dy^{3+}) phosphor for TLD applications, *J. Molec. Struct.* **1225** (2021) 129129.
51. S. Dhas, S. Suresh, A. Rita et al., Effect of annealing on the photoluminescence and thermoluminescence properties of Eu^{2+} doped $BaSO_4$ microgravels, *J. Mater. Sci: Mater. Electron.* **31** (2020) 11113-11122.
52. A.R. Kadam, S.B. Dhoble, G.C. Mishra et al, Combustion assisted spectroscopic investigation of Dy^{3+} activated $SrYAl_3O_7$ phosphor for LED and TLD applications, *J. Mol. Struct.* **1233** (2021) 130150.
53. G. Kitis, R. Chen and V Pagonis, Thermoluminescence glow-peak shape methods based on mixed order kinetics, *Phys. Status Solidi (a)* **205** (2008) 1181-1189.
54. P. Dewangan, D. Bisen, N. Brahme et al., Structural characterization and luminescence properties of Dy^{3+} doped $Ca_3MgSi_2O_8$ phosphors, *J. Alloy. Comp.* **777** (2019) 423-433.
55. N. Trindade, M. Magalhaes, M. Nunes et al., Thermoluminescence of UV-irradiated α-Al_2O_3:C,Mg, *J. Lumin.* **223** (2020) 117195.
56. I. Sahu, D. Bisen, N. Brahme et al., Luminescence studies of dysprosium doped strontium aluminate white light emitting phosphor by combustion route, *J. Mater. Sci: Mater. Electron.* **26** (2015) 8824-8839.
57. G. banjare, D. Bisen, N. Brahme et al., Thermoluminescence studies of Dy^{3+}-doped calcium barium orthosilicate codoped with Li^+ ion, *J. Ther. Anal. Calori.* **139** (2020) 1577-1583.
58. J. Kalita and G. Wary, Thermoluminescence study of X-ray and UV irradiated natural calcite and analysis of its trap and recombination level, *Spectrochim Acta A Mol. Biomol. Spectrosc.* **5** (2014) 99-103.
59. S. Sharma, n. Brahme, D. Bisen et al., Study on photoluminescence and thermoluminescence properties of UV-irradiated $CaSrAl_2SiO_7$:Ce^{3+} phosphors, *J. Mater. Sci: Mater. Electron*. **29** (2018) 1412-1219.

60. R. Tamrakar, K. Upadhyay and D. Bisen, 3T1R model and tuning of thermoluminescence intensity by optimization of dopant concentration in monoclinic $Gd_2O_3:Er^{3+};Yb^{3+}$ co-doped phosphor, *Phys. Chem. Chem. Phys.* **19** (2017) 14680-14694.
61. P. Gonzalez, O. Avila, L. Escobar-Alarcon et al., Luminescence and kinetics parameters of high sensitivity MgB_4O_7 phosphor co-doped with Tm and Dy, *Appl. Radia. Isotop.* **175** (2021) 109811.